Void Shape and Orientation Effects on Anisotropic Porous Material Formability

Muhammad Waqar Nasir[1], Shuraim Muzammil[1], Hocine Chalal[2], Farid Abed-Meraim[2]

[1] Department of Mechanical Engineering, University of Engineering and Technology, Lahore 54000, Pakistan.
[2] Université de Lorraine, CNRS, Arts et Métiers Institute of Technology, LEM3, F-57000 Metz, France.

Abstract

This study investigates the influence of void shape and orientation on the Forming Limit Diagrams (FLDs) of porous materials with non-quadratic anisotropy. The constitutive framework integrates the Gologanu–Leblond–Devaux (GLD) damage model, which accounts for void morphology, with Barlat's YLD-2004-18p non-quadratic yield criterion to capture metal matrix plastic anisotropy. The combined GLD-YLD model is further coupled with the Marciniak–Kuczyński (M–K) imperfection approach to predict FLDs for anisotropic sheet metals. Results demonstrate that void morphology considerably affects formability, with prolate (needle-like) voids enhancing material ductility, as compared to oblate (plate-like) voids, while spherical voids yield an intermediate behavior. Furthermore, the study highlights that the impact of material orientation on formability involves a complex interplay of several factors, which include coupled matrix-induced and void-shape-induced anisotropy, the relative angle between the rolling direction and void orientation, and void nucleation mechanism. The model predictive capabilities are assessed against experimental FLD data for two aluminum alloys. Although these alloys show only slight sensitivity to void morphology, due to low porosity, the void shape-dependent anisotropic GLD-YLD model better captures the experimental trends as compared to the undamaged isotropic von Mises model, which overly overestimates formability on the right-hand side of FLD. The role of isotropic hardening is also examined, which shows that higher hardening improves formability, and the effect is smallest for oblate voids under balanced biaxial loading. These findings underscore the importance of incorporating both damage and matrix-induced anisotropy in constitutive modeling for accurate FLD prediction.

Keywords

Forming Limit Diagrams (FLDs), Anisotropic Porous Plasticity, Sheet Metal Formability, Gologanu–Leblond–Devaux (GLD) Model, Marciniak and Kuczyński (M–K) Approach, Void Morphology, Void Orientation

1. Introduction

Sheet metal forming is a key manufacturing process widely employed in various industries, including aerospace, automotive, electronics and construction, highlighting its importance and industrial value. This process enables the efficient and precise production of complex geometries and structures, ensuring reliability and quality. During metal forming, the material is subjected to substantial amount of stress and strain, resulting in significant plastic deformation of the sheet. Such deformation must be controlled to prevent tearing, wrinkling, or cracking, which can ultimately lead to plastic instabilities and process failure. Therefore, safe design of sheet-metal components requires strict prevention of excessive localized deformation.

Localized deformation in metals can be monitored and controlled by accurately predicting their formability limits. These limits are influenced by several factors including anisotropic material behavior, strain hardening capacity, void shape, void size and growth rate, sheet thickness, through-thickness stresses, strain rate, temperature, and surface roughness. It is essential to understand the influence of these parameters for improving the productivity and reliability of the forming processes. A widely utilized method for characterizing sheet metal formability is the forming limit diagram (FLD) [1,2], which graphically represents the major and minor necking strains under in-plane biaxial stretching. Conventionally, FLDs are determined experimentally using standardized methods, such as the Nakajima and Erichsen tests [3,4]. However, these experiments are time-consuming and costly. As an alternative, FLDs can be predicted numerically by coupling constitutive models with appropriate necking or instability criteria.

Accurate modeling of material response under diverse loading conditions requires the incorporation of several physically-based phenomena within the constitutive framework. Key aspects include isotropic and kinematic hardening, plastic anisotropy and material softening. One of the pioneering works in this field is the Gurson damage model, which was originally developed based on micromechanics of representative volume element considering spherical voids [5]. In this model, porosity was the only microstructural variable serving as a measure of material damage. During deformation, porosity evolves due to void growth phenomenon, thereby inducing softening in the material response. Later, Chu and Needleman [6] and Tvergaard [7] modified the Gurson model by incorporating void nucleation and void coalescence mechanisms, in addition to void growth.

Over the past four decades, the Gurson model has been extensively enhanced through the inclusion of isotropic and kinematic hardening [8,9], void size effects [10,11], void anisotropy [12,13], void coalescence mechanisms [14], lode parameter [15], and the influence of shear stresses on porosity evolution [16-18]. Pardoen et al. [19] extended the Gurson framework to simulate fracture in porous ductile materials, while more recent studies [20,21] focused on improving the damage parameter identification process in the GTN model. Aravas and Xenos [22] examined explicit and implicit gradient

plasticity models, showing that non-local models can enhance stability and reduce mesh dependence when appropriate material length scales are introduced. Despite these advances, the original Gurson model assumes an isotropic and homogeneous matrix material around voids, limiting its accuracy for porous materials exhibiting grain-scale anisotropy. To address this, Wang et al. [23] developed a statistical yield model that captures the effect of grain anisotropy in porous materials.

In the original and most subsequent modifications of the Gurson model, voids were assumed to remain spherical even after plastic deformation, which is only a first-order approximation for modeling porous materials. To overcome this limitation, Gologanu and coworkers [24-26] extended the Gurson model by introducing Gologanu–Leblond–Devaux (GLD) model, which accounts for non-spherical voids. The GLD model has since been applied by several researchers to investigate the effects of void spacing and void shape on coalescence mechanism [27-29]. Benzerga and coworkers [30-32] proposed a micro-mechanical model to examine the influence of void-related mechanisms on ductile fracture. Gao et al. [33] investigated the influence of void volume fraction, void pattern, void shape and spacing using finite element analysis. Enakoutsa and Li [34] implemented the GLD model in finite element simulations of steel fracture tests, whereas Madou and Leblond [35,36] further modified it for plastic porous solids containing arbitrary ellipsoidal cavities. Their work was validated through finite element analysis for yield surfaces corresponding to eight different void geometries [37,38]. Roubaud et al. [39] extended the model by incorporating mixed isotropic and kinematic hardening, alongside void shape effects, which is crucial for capturing ratcheting and cyclic loading under low stress triaxiality. More recently, Xenos et al. [40] developed a fully explicit elasto-plastic Gurson-type model for porous materials with randomly oriented spheroidal voids based on the homogenization theory.

Several researchers have examined the influence of void orientation, shape, and loading conditions on void evolution in ductile materials. Hosseini et al. [41] analyzed the effect of material orientation on void growth using finite element simulations, where material behavior was described by an orthotropic elastoplastic constitutive model based on Barlat's YLD-2004-18p yield criterion [42]. Their results showed that void shape evolution strongly depends on material orientation and angular misalignment. Kumar et al. [43] developed a model to predict void shape and size under pure shear, combined tension-shear, and compression-shear loading conditions. Usman et al. [44] investigated void growth at different aspect ratios of elliptical voids under uniaxial and biaxial deformation, revealing that void orientation significantly affects the response of voided ductile materials. Another work [45] further demonstrated that voids with larger surface area exhibit higher growth rate, while biaxial loading promotes greater strain hardening compared to uniaxial loading. In addition, the GLD model has been widely used in the literature for predicting FLDs, particularly through its coupling with various anisotropic yield criteria and extensions to account for void shape effects and ductile fracture mechanisms (see, e.g., [46-53]). More specifically, Son and Kim [46] predicted the FLD of anisotropic metal sheets containing

axisymmetric prolate ellipsoidal cavities by coupling the GLD yield function with Barlat and Lian's [54] non-quadratic anisotropic yield criterion.

While the GLD model and its extensions provide an effective constitutive description for porous materials, accurate prediction of forming limits additionally requires an appropriate necking criterion. In this regard, Marciniak and Kuczyński [55] were the first to propose an analytical framework (known as M–K model), based on the assumption of initial local inhomogeneity, which enabled the prediction of sheet metal forming limits under in-plane biaxial stretching. However, the model initially failed to accurately predict limit strain results for negative strain-path ratios. Subsequently, improvements included the introduction of band angle inclination [56], extensions to visco-plastic materials [57] and the consideration of imperfection band rotation during plastic deformation [58,59]. Over time, the M–K model has been successfully coupled with various constitutive descriptions, such as ductile damage models, advanced physically-based phenomenological approaches, and polycrystalline yield surfaces, for reliable FLD prediction (see, e.g., [60,61]).

An alternative approach for predicting localized necking is based on bifurcation theory, wherein the contribution of Stören and Rice [62] is particularly noteworthy. They incorporated the J_2 deformation theory of plasticity for predicting localized necking across the full range of FLD. Several researchers have also proposed numerical approaches for predicting the onset of localized necking (see, e.g., [63-66]). However, due to their computational complexity and other limitations, these models are less frequently employed compared to the analytical M–K model. Notably, it has also been shown that the M–K model converges to the bifurcation theory-based localization criterion when the imperfection size in the M–K model tends to zero [67].

Furthermore, the effect of different material parameters on FLDs has been extensively studied in the literature. Mansouri et al. [68] studied the influence of GTN damage parameters and found that they significantly affect limit strains when compared with dense matrix hardening parameters. In a follow-up study, the same group [69] analyzed the combined effects of isotropic hardening and void nucleation, concluding that isotropic hardening parameters strongly influence formability when stress-controlled nucleation is considered. The effect of anisotropy on formability has also received considerable attention in recent years [70–75], with results consistently showing that the shape of the yield surface is a critical factor in FLD prediction within the M–K framework. Djavanroodi et al. [76] compared FLDs of anisotropic aluminum AA7075 and titanium Ti-6Al-4V alloys. They reported that the aluminum alloy had smaller strain hardening exponent and anisotropy factor, leading to lower value of major strain and less resistance to thinning. Additionally, the Gurson model has been applied within the framework of non-associated flow rules [77] for the prediction of FLDs.

The effects of stress triaxiality and the corresponding Lode parameter on formability have also been widely studied (see, e.g., [15,16,78-80]). These studies indicate that the Lode parameter has a significant

effect on material fracture and failure behavior. Nasir et al. [81] investigated the effect of void size on FLDs by combining the Dormieux and Kondo [11] constitutive model with the Rice bifurcation criterion. It was determined that smaller voids lead to higher ductility limits, with the effect being more significant for high initial porosity. Other studies have highlighted that through-thickness compressive stresses, in addition to in-plane stresses, play an important role during hydroforming processes [82–84], with results showing an upward shift in FLDs when compressive normal stresses are applied. Moreover, the effect of through-thickness shear stress on the material formability and fracture has also been examined in the recent years [85,86]. In parallel, artificial neural networks (ANN) and machine learning methods have been increasingly applied to predict FLDs of thin sheet metals [87–92].

Despite these extensive efforts, to the best of the authors' knowledge, no prior study has analyzed the effect of void shape on FLDs across the full range of strain path ratios, while considering both prolate and oblate void geometries. Furthermore, the presence of non-spherical void shapes introduces an additional mechanism affecting the overall anisotropic material behavior. In addition, the potential effect of misalignment between the rolling direction of the anisotropic matrix material in the representative volume element (RVE) of the GLD model and the major axis of ellipsoidal voids has not yet been addressed in the literature.

This study develops a constitutive framework for predicting FLDs of anisotropic porous materials. The Gologanu–Leblond–Devaux (GLD) damage model is combined with Barlat's non-quadratic YLD-2004-18p yield criterion to represent void morphology and matrix material anisotropy. The framework is further integrated with the Marciniak–Kuczyński (M–K) imperfection approach and numerically implemented in MATLAB. Validation is conducted against established damage models, such as the GTN model, and reference results reported in the literature. The validated framework is then applied to study the effects of void morphology, void orientation, misalignment, and isotropic hardening. Finally, the model predictive capabilities are evaluated using FLD data for two aluminum alloys, demonstrating high accuracy of the constitutive framework. The overall findings confirm that accounting for both damage-induced and matrix-induced anisotropy is essential for reliable prediction of FLDs. The paper is organized as follows: Section 2 describes the constitutive equations, yield criterion, and numerical implementation. Section 3 presents validation and sensitivity analysis, while Section 4 introduces the material and variable parameters. Section 5 discusses the results, followed by the limitations and future perspectives in Section 6. Finally, the conclusions are summarized in Section 7.

Nomenclature

c	focal distance
w	aspect ratio

$e_1,\ e_2$	eccentricities of void and RVE
S	logarithmic aspect ratio
(P)	shorthand notation for prolate voids
(O)	shorthand notation for oblate voids
Φ_{GLD}	GLD yield surface
$\Phi_{GLD+YLD}$	coupled GLD-YLD yield surface
f	total void volume fraction (also called porosity)
f_0	initial void volume fraction (also called initial porosity)
$\boldsymbol{\Sigma}$	macroscopic Cauchy stress tensor
$\boldsymbol{\Sigma}'$	deviatoric part of the macroscopic Cauchy stress tensor $\boldsymbol{\Sigma}$
Σ_h	modified hydrostatic part of the macroscopic Cauchy stress tensor $\boldsymbol{\Sigma}$
Σ_{eq}	macroscopic equivalent stress
Σ_m	macroscopic mean stress
$\bar{\sigma}$	yield stress of the fully dense matrix
$\mathbf{I}$	second-order identity tensor
$\bar{\varepsilon}^p$	equivalent plastic strain of the dense matrix
$\mathbf{D}$	total macroscopic strain rate tensor
$\mathbf{D}^p$	macroscopic plastic strain rate tensor
h	plastic hardening modulus of the dense matrix
K, ε_0, n	Swift's hardening parameters of the dense matrix
$\dot{f}_G$	porosity evolution due to void growth
$\dot{f}_N$	porosity evolution due to void nucleation
ψ	volume fraction of cavities that are likely to nucleate
ε_N	equivalent plastic strain for which half of inclusions have nucleated

s_N	standard deviation on ε_N
q_1, q_2, q_3	void interaction material parameters
f^*	effective porosity (modified void volume fraction for void coalescence)
f_{cr}	critical porosity for void coalescence
δ_{GTN}	accelerating factor for void coalescence
$\dot{\lambda}$	plastic multiplier
T	stress triaxiality ratio
$\tilde{\mathbf{s}}'$, $\tilde{\mathbf{s}}''$	transformed deviatoric stress tensors
$\mathbf{C}^e$	fourth-order elasticity tensor
$\mathbf{C}^{ep}$	analytical elastic–plastic tangent modulus
B	imperfection band
H	homogeneous zone
$\dot{\bar{\varepsilon}}^{p^B}$, $\dot{\bar{\varepsilon}}^{p^H}$	equivalent plastic strain rate inside the imperfection band and homogeneous zone, respectively
h_i^B, h_i^H	initial thickness of imperfection band and homogeneous zone, respectively
$\mathbf{G}$	velocity gradient tensor
$\dot{\mathbf{c}}$	jump amplitude vector
$\mathbf{n}$	unit vector normal to the imperfection band at time t
ρ	strain-path ratio
z	geometric imperfection factor at time t
z_0	initial geometric imperfection factor
β	orientation of the imperfection band with respect to the major principal strain axis at time t
β_0	initial orientation of the imperfection band with respect to the major principal strain axis

θ	void orientation angle with respect to the minor principal strain axis
Δt	time step for loading increment
$\mathbf{y}$	vector incorporating all internal variables for the GLD-YLD damage model

Notations

$\bullet_{ij}$	component *ij* of tensor quantity $\bullet$
$\bullet_t$	value of quantity $\bullet$ at the beginning of loading increment
$\bullet_{t+1}$	value of quantity $\bullet$ at the end of loading increment
$\bullet^B$	value of quantity $\bullet$ inside the imperfection band
$\bullet^H$	value of quantity $\bullet$ inside the homogeneous zone

Mathematical operators

Vector and tensor fields are designated by bold letters and symbols

Scalar variables and parameters are represented by italic thin letters and symbols

Einstein's convention of summation over repeated indices is adopted

$\bullet \cdot \bullet$	Inner product between two second-order tensors ($=\bullet_{ij}\bullet_{jk}$)
	Inner product between a second-order tensor and a vector ($=\bullet_{ij}\bullet_{j}$)
$\bullet : \bullet$	Double contraction between two second-order tensors ($=\bullet_{ij}\bullet_{ij}$)
	Double contraction between fourth- and second-order tensors ($=\bullet_{ijkl}\bullet_{kl}$)
$\bullet \otimes \bullet$	Tensor product of two second-order tensors ($=\bullet_{ij}\bullet_{kl}$)

2. Constitutive modeling

This section presents a comprehensive constitutive framework to accurately capture the combined effects of void morphology, plastic anisotropy, and work hardening on the formability of porous anisotropic sheet metals. The framework begins with the GLD model, which extends classical porous plasticity theory by explicitly accounting for the influence of void shape and orientation on the overall material response. To represent the anisotropic plastic behavior of the metal matrix, Barlat's YLD-

2004-18p non-quadratic anisotropic yield criterion is integrated with the GLD formulation, enabling a precise description of directional yielding under complex loading conditions. Furthermore, the derivation of the plastic multiplier and elastic–plastic tangent modulus is presented, which forms the foundation for consistent numerical implementation and ensures stable convergence during simulations. In order to predict forming limit diagrams, the Marciniak–Kuczyński (M–K) imperfection approach is adopted as the localized necking criterion, which links material constitutive behavior with the onset of plastic instability. Finally, the complete constitutive model, including all coupled effects, is implemented in MATLAB to provide an efficient computational framework for investigating the impact of void morphology, matrix material anisotropy, and work hardening on the sheet metal formability.

2.1. GLD model

The GLD model was originally developed to accurately describe the mechanical behavior of porous ductile materials. Unlike the original Gurson model, which considered only spherical cavities for the description of porous material behavior, the GLD model accounts for both prolate [24] and oblate [25] ellipsoidal void shapes. The representative volume elements containing confocal ellipsoidal voids, as considered in the GLD model, are presented in Appendix A, together with the expressions for the void aspect ratio (w) and the eccentricities of both the void and the RVE. The macroscopic yield function of the GLD model is defined as follows:

$$\Phi_{GLD}=\frac{C}{\bar{\sigma}^2}\left\|\boldsymbol{\Sigma}'+\eta\Sigma_h\mathbf{X}\right\|^2+2q(g+1)(g+f)\cosh\left(\kappa\frac{\Sigma_h}{\bar{\sigma}}\right)-(g+1)^2-q^2(g+f)^2=0\ , \tag{1}$$

where $\|\mathbf{T}\|=\sqrt{\frac{3}{2}\mathbf{T}:\mathbf{T}}$ denotes the von Mises norm of a given second-order tensor $\mathbf{T}$, $\boldsymbol{\Sigma}'$ is the deviatoric part of the Cauchy stress tensor $\boldsymbol{\Sigma}$, $\bar{\sigma}$ is the yield strength, and f is the porosity. The quantities C, η, g, q and κ are functions of S and f, where $S=ln(w)$. The functional dependencies of these quantities are defined in Appendix B. The second-order tensor $\mathbf{X}$ and the modified hydrostatic stress Σ_h are defined as (see, e.g., [24,28,93]):

$$\mathbf{X}=\frac{2}{3}(\boldsymbol{e}_y\otimes\boldsymbol{e}_y)-\frac{1}{3}(\boldsymbol{e}_x\otimes\boldsymbol{e}_x)-\frac{1}{3}(\boldsymbol{e}_z\otimes\boldsymbol{e}_z), \tag{2}$$

$$\Sigma_h=\alpha_2(\Sigma_{xx}+\Sigma_{zz})+(1-2\alpha_2)\Sigma_{yy}\ . \tag{3}$$

The expression of factor α_2 is presented in Appendix B. There are three internal variables in the GLD model, i.e., f, S and $\bar{\sigma}$. The evolution of $\bar{\sigma}$ follows the Swift isotropic hardening law, defined as $\bar{\sigma}=K(\bar{\varepsilon}^p+\varepsilon_0)^n$, where $\bar{\varepsilon}^p$ is the equivalent plastic strain of the fully dense matrix material, while

K, ε_0 and *n* are the isotropic hardening parameters. By adopting the equivalence principle in the plastic work rate, the relationship between the equivalent plastic strain rate and the macroscopic plastic strain rate tensor $\mathbf{D}^p$ can be derived as follows:

$$(1-f)\bar{\sigma}\,\dot{\bar{\varepsilon}}^p = \boldsymbol{\Sigma} : \mathbf{D}^p . \tag{4}$$

The evolution equations of the three internal variables f, S and $\bar{\sigma}$ are presented in Appendix C.

2.2. Barlat's YLD-2004-18p yield criterion

In the formulation of the original GLD model, the dense matrix material behavior was assumed to be isotropic, i.e., it follows the von Mises norm of the corrected deviatoric stress. However, most sheet metals exhibit anisotropic behavior in nature. To address this, the present study heuristically extends the GLD model to account for anisotropy. Barlat et al. [42] extended their YLD-1991 yield function to YLD-2004-18p criterion, which accurately captures the anisotropy in thin sheet metals. This yield criterion was derived through two linear transformations of the Cauchy stress tensor and involves 19 anisotropy material parameters. The expression of this yield criterion is given as follows:

$$\Sigma_{eq}(\boldsymbol{\Sigma}) = \left(\frac{1}{4}\right)^{\frac{1}{a}} \left[\begin{array}{l} \left|\tilde{S}'_1 - \tilde{S}''_1\right|^a + \left|\tilde{S}'_1 - \tilde{S}''_2\right|^a + \left|\tilde{S}'_1 - \tilde{S}''_3\right|^a + \left|\tilde{S}'_2 - \tilde{S}''_1\right|^a + \left|\tilde{S}'_2 - \tilde{S}''_2\right|^a + \left|\tilde{S}'_2 - \tilde{S}''_3\right|^a + \\ \qquad \left|\tilde{S}'_3 - \tilde{S}''_1\right|^a + \left|\tilde{S}'_3 - \tilde{S}''_2\right|^a + \left|\tilde{S}'_3 - \tilde{S}''_3\right|^a \end{array} \right]^{\frac{1}{a}}$$

. (5)

In the relation above, $\tilde{S}'_p$ and $\tilde{S}''_p$ for *p*=1, 2, 3 are the three principal values of two linearly transformed deviatoric stress tensors $\tilde{\mathbf{s}}'$ and $\tilde{\mathbf{s}}''$ respectively. The transformation matrices are expressed in the following equations:

$$\tilde{\mathbf{s}}' = \mathbf{C}'\mathbf{T}\boldsymbol{\Sigma} = \mathbf{L}'\boldsymbol{\Sigma} \text{ and } \tilde{\mathbf{s}}'' = \mathbf{C}''\mathbf{T}\boldsymbol{\Sigma} = \mathbf{L}''\boldsymbol{\Sigma}, \tag{6}$$

where

$$\mathbf{C}'=\begin{bmatrix} 0 & -c'_{12} & -c'_{13} & 0 & 0 & 0 \\ -c'_{21} & 0 & -c'_{23} & 0 & 0 & 0 \\ -c'_{31} & -c'_{32} & 0 & 0 & 0 & 0 \\ 0 & 0 & 0 & -c'_{66} & 0 & 0 \\ 0 & 0 & 0 & 0 & -c'_{55} & 0 \\ 0 & 0 & 0 & 0 & 0 & -c'_{44} \end{bmatrix};\quad \mathbf{C}''=\begin{bmatrix} 0 & -c''_{12} & -c''_{13} & 0 & 0 & 0 \\ -c''_{21} & 0 & -c''_{23} & 0 & 0 & 0 \\ -c''_{31} & -c''_{32} & 0 & 0 & 0 & 0 \\ 0 & 0 & 0 & -c''_{66} & 0 & 0 \\ 0 & 0 & 0 & 0 & -c''_{55} & 0 \\ 0 & 0 & 0 & 0 & 0 & -c''_{44} \end{bmatrix};$$

$$\mathbf{T}=\frac{1}{3}\begin{bmatrix} 2 & -1 & -1 & 0 & 0 & 0 \\ -1 & 2 & -1 & 0 & 0 & 0 \\ -1 & -1 & 2 & 0 & 0 & 0 \\ 0 & 0 & 0 & 3 & 0 & 0 \\ 0 & 0 & 0 & 0 & 3 & 0 \\ 0 & 0 & 0 & 0 & 0 & 3 \end{bmatrix}. \tag{7}$$

In the above equations, c'_{12}, c'_{13}, c'_{21}, c'_{23}, c'_{31}, c'_{32}, c'_{44}, c'_{55}, c'_{66}, c''_{12}, c''_{13}, c''_{21}, c''_{23}, c''_{31}, c''_{32}, c''_{44}, c''_{55}, c''_{66} and a are the 19 material anisotropy parameters. It is important to note that similar to YLD-1991, the YLD-2004-18p yield function becomes equivalent to the von Mises isotropic yield function when all coefficients are equal to 1 and a=2 or 4.

For coupling the YLD anisotropic material response and the GLD void-shape dependent model, the yield function Φ, presented in Eq. (1), is rewritten as:

$$\Phi_{GLD+YLD}=\frac{C}{\bar{\sigma}^2}\left[\left(\frac{1}{4}T_{YLD}\right)^{1/a}\right]^2+2q(g+1)(g+f)\cosh\left(\kappa\frac{\Sigma_h}{\bar{\sigma}}\right)-(g+1)^2-q^2(g+f)^2=0\ , \tag{8}$$

where the term T_{YLD} is calculated as follows. Firstly, the corrected, linearly transformed deviatoric stress tensors, i.e., $\tilde{\mathbf{p}}'$ and $\tilde{\mathbf{p}}''$, are calculated using the following relationships:

$$\tilde{\mathbf{p}}'=\mathbf{L}'\boldsymbol{\Sigma}+\eta\Sigma_h\mathbf{X}, \tag{9}$$

and

$$\tilde{\mathbf{p}}''=\mathbf{L}''\boldsymbol{\Sigma}+\eta\Sigma_h\mathbf{X}. \tag{10}$$

Secondly, the principal values $\tilde{P}'_1$, $\tilde{P}'_2$, $\tilde{P}'_3$ and $\tilde{P}''_1$, $\tilde{P}''_2$, $\tilde{P}''_3$ are calculated for the $\tilde{\mathbf{p}}'$ and $\tilde{\mathbf{p}}''$ tensors, respectively. Finally, the term T_{YLD} is calculated as follows:

$$\begin{aligned} T_{YLD}=&\left|\tilde{P}'_1-\tilde{P}''_1\right|^a+\left|\tilde{P}'_1-\tilde{P}''_2\right|^a+\left|\tilde{P}'_1-\tilde{P}''_3\right|^a+\left|\tilde{P}'_2-\tilde{P}''_1\right|^a+\left|\tilde{P}'_2-\tilde{P}''_2\right|^a+\left|\tilde{P}'_2-\tilde{P}''_3\right|^a+ \\ &\left|\tilde{P}'_3-\tilde{P}''_1\right|^a+\left|\tilde{P}'_3-\tilde{P}''_2\right|^a+\left|\tilde{P}'_3-\tilde{P}''_3\right|^a. \end{aligned} \tag{11}$$

2.3. *Determination of the plastic multiplier and the elastic–plastic tangent modulus*

In this subsection, the plastic multiplier $\dot{\lambda}$ and the elastic–plastic tangent modulus $\mathbf{C}^{ep}$ for the GLD-YLD coupled model are derived using the consistency condition, i.e., $\dot{\Phi}=0$:

$$\dot{\Phi}=(\frac{\partial\Phi}{\partial\boldsymbol{\Sigma}}):\dot{\boldsymbol{\Sigma}}+(\frac{\partial\Phi}{\partial\bar{\sigma}})\dot{\bar{\sigma}}+(\frac{\partial\Phi}{\partial f^{*}})\dot{f}^{*}+(\frac{\partial\Phi}{\partial S})\dot{S}=0, \tag{12}$$

where $\frac{\partial\Phi}{\partial\boldsymbol{\Sigma}}$, $\frac{\partial\Phi}{\partial\bar{\sigma}}$, $\frac{\partial\Phi}{\partial f^{*}}$ and $\frac{\partial\Phi}{\partial S}$ represent the partial derivatives of Φ with respect to the state variables, i.e., $\boldsymbol{\Sigma}$, $\bar{\sigma}$, f and S. In the above Eq. (12), the Cauchy stress rate tensor is given by the following hypo elastic law expressed in the corotational material frame:

$$\dot{\boldsymbol{\Sigma}}=\mathbf{C}^{e}:(\mathbf{D}-\mathbf{D}^{p})=\mathbf{C}^{e}:(\mathbf{D}-\dot{\lambda}\frac{\partial\Phi}{\partial\boldsymbol{\Sigma}})=\mathbf{C}^{ep}:\mathbf{D}. \tag{13}$$

In the above equation, $\mathbf{C}^{e}$ represents the fourth-order tensor of the elasticity constants and $\mathbf{D}$ is the macroscopic strain rate tensor. By substituting Eqs. (4), (13) and the evolution equations of the three internal variables (i.e., f, S and $\bar{\sigma}$) from Appendix C into Eq. (12), the final expression of the plastic multiplier $\dot{\lambda}$ is derived as follows:

$$\dot{\lambda}=\frac{\frac{\partial\Phi}{\partial\boldsymbol{\Sigma}}:\mathbf{C}^{e}:\mathbf{D}}{H_{\lambda}}, \tag{14}$$

where

$$H_{\lambda}=\left[\begin{array}{l}\left(\frac{\partial\Phi}{\partial\boldsymbol{\Sigma}}:\mathbf{C}^{e}:\frac{\partial\Phi}{\partial\boldsymbol{\Sigma}}\right)-\frac{\partial\Phi}{\partial S}\left(\frac{3}{2}\xi_{1}\left\{\frac{\partial\Phi}{\partial\boldsymbol{\Sigma}}:\mathbf{X}\right\}+\xi_{2}\left\{\frac{\partial\Phi}{\partial\boldsymbol{\Sigma}}:\mathbf{I}\right\}\right)- \\ \frac{\partial\Phi}{\partial f^{*}}\delta_{GTN}\left(A_{N}\frac{\boldsymbol{\Sigma}:\frac{\partial\Phi}{\partial\boldsymbol{\Sigma}}}{(1-f)\bar{\sigma}}+(1-f)\left\{\frac{\partial\Phi}{\partial\boldsymbol{\Sigma}}:\mathbf{I}\right\}\right)-\frac{\partial\Phi}{\partial\bar{\sigma}}\left(h\frac{\boldsymbol{\Sigma}:\frac{\partial\Phi}{\partial\boldsymbol{\Sigma}}}{(1-f)\bar{\sigma}}\right)\end{array}\right], \tag{15}$$

where $\mathbf{I}$ is the second-order identity tensor. Finally, substituting the expression of $\dot{\lambda}$ into the hypo elastic law given by Eq. (41), the elastic–plastic tangent modulus is calculated as:

$$\mathbf{C}^{ep}=\mathbf{C}^{e}-\frac{\left(\mathbf{C}^{e}:\frac{\partial\Phi}{\partial\boldsymbol{\Sigma}}\right)\otimes\left(\frac{\partial\Phi}{\partial\boldsymbol{\Sigma}}:\mathbf{C}^{e}\right)}{H_{\lambda}}. \tag{16}$$

2.4. *Localized necking criterion*

The M–K imperfection approach [56] was developed to predict localized necking in thin sheet metals. In this model, an initial imperfection in the sheet metal is considered in the form of a narrow

band, which either have geometric imperfection, material imperfection, or both. In the original M–K imperfection approach, the imperfection band was considered perpendicular to the major principal strain axis, leading to higher forming limit strain values. Hutchinson and Neale [58] modified the M–K model by allowing the imperfection band to rotate from an angle β_0 to the major principal strain axis. Since the imperfection band is considered weaker than the homogenous zone, the strains in this imperfection zone remain larger during in-plane biaxial stretching. Localization is assumed to occur when the ratio of equivalent plastic strain rate inside the imperfection band to the homogenous zone, i.e., $\dot{\bar{\varepsilon}}^{p^B} / \dot{\bar{\varepsilon}}^{p^H}$, exceeds a certain critical value. Fig.1 below illustrates the sheet metal model considered for the implementation of the M–K imperfection approach. In this figure, *H* represents the homogenous material, while *B* represents the imperfection band.

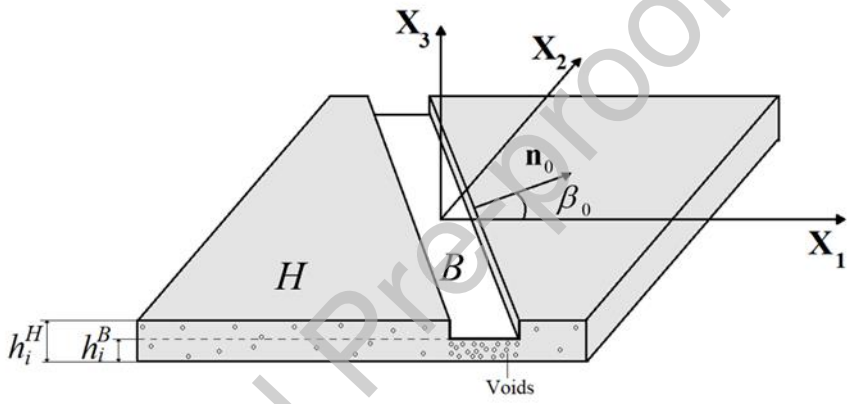

Fig. 1. Schematic representation of the initial imperfection band in the M–K imperfection approach.

The initial geometric imperfection factor is defined as:

$$z_0 = \frac{h_i^B}{h_i^H}. \tag{17}$$

In the above equation, quantities inside and outside the imperfection band are represented by the superscripts *B* and *H*, respectively. Further details on the M–K imperfection approach are discussed in [67]. Following the condition of kinematic compatibility, the velocity gradients in the imperfection band $\mathbf{G}^B$ and in the homogeneous zone $\mathbf{G}^H$ are related as:

$$\mathbf{G}^B = \mathbf{G}^H + \dot{\mathbf{c}} \otimes \mathbf{n}, \tag{18}$$

where $\dot{\mathbf{c}}$ is the jump amplitude vector, and $\mathbf{n}$ is the unit vector normal to the imperfection band in the current configuration. The strain path ratio is defined as:

$$\rho = \frac{\dot{\varepsilon}_{22}^{H}}{\dot{\varepsilon}_{11}^{H}} = \frac{G_{22}^{H}}{G_{11}^{H}};\ -0.5 \le \rho \le 1. \tag{19}$$

In the above relation, $\rho = -0.5$, $\rho = 0$, and $\rho = 1$ represent uniaxial tension, plane-strain tension, and balanced biaxial tension, respectively. The velocity gradient in the homogenous zone is given as:

$$\mathbf{G}^{H} = \begin{bmatrix} \dot{\varepsilon}_{11}^{H} & 0 & 0 \\ 0 & \rho\dot{\varepsilon}_{11}^{H} & 0 \\ 0 & 0 & G_{33}^{H} \end{bmatrix}. \tag{20}$$

By substituting Eq. (20) in Eq. (18):

$$\mathbf{G}^{B} = \begin{bmatrix} \dot{\varepsilon}_{11}^{H} + \dot{c}_1 n_1 & \dot{c}_1 n_2 & 0 \\ \dot{c}_2 n_1 & \rho\dot{\varepsilon}_{11}^{H} + \dot{c}_2 n_2 & 0 \\ 0 & 0 & G_{33}^{B} \end{bmatrix}. \tag{21}$$

The components of the velocity gradients G_{33}^{H} and G_{33}^{B} are calculated such that the plane-stress conditions are satisfied, i.e., $\Sigma_{33}^{H} = 0$ and $\Sigma_{33}^{B} = 0$. The equilibrium of forces across the imperfection band can be expressed by the following equation:

$$(z\boldsymbol{\Sigma}^{B} - \boldsymbol{\Sigma}^{H}) \cdot \mathbf{n} = \mathbf{0}. \tag{22}$$

In the above equation, z is the value of the geometric imperfection factor in the deformed current configuration, which can be expressed as:

$$z = \frac{h^{B}}{h^{H}} = \frac{h_i^{B} \exp(\varepsilon_{33}^{B})}{h_i^{H} \exp(\varepsilon_{33}^{H})} = z_0 \exp(\varepsilon_{33}^{B} - \varepsilon_{33}^{H}), \tag{23}$$

where z_0 is the initial value of the geometric imperfection factor. Note that the imperfection band rotates during the applied loading. The evolution of the band inclination angle β is given according to Nanson's formula:

$$\tan(\beta) = \tan(\beta_0) \exp(\varepsilon_{11}^{H} - \varepsilon_{22}^{H}), \tag{24}$$

where β_0 is the initial orientation of the imperfection band with respect to the major principal strain axis (see Fig. 1).

2.5. Numerical implementation

In this study, the GLD model, coupled with the M–K imperfection approach for FLD prediction, is implemented into MATLAB software. As illustrated in Fig. 1, the homogenous zone of the sheet metal is subjected to proportional in-plane biaxial strains, with strain path ratios (ρ) ranging from –0.5 to 1.

For each strain path ratio, the initial band orientation angle (β_0) is varied between 0° and 90°. For each combination of ρ and β_0, the simulation is executed using an explicit time integration scheme, where stress, strain and other internal variables are updated for each loading increment. The band orientation angle is further allowed to evolve during the simulation according to Eq. (24). The simulation terminates when the ratio $\dot{\bar{\varepsilon}}^{p^B} / \dot{\bar{\varepsilon}}^{p^H}$ exceeds the critical value of 10. The corresponding principal strain values in the homogenous zone, i.e., ε_{11}^H and ε_{22}^H, are taken as the critical strains for the selected value of β_0. This procedure is repeated for all the values of initial band orientation angle, and the smallest critical major strain is considered as the forming limit strain for the given strain path ratio. In this study, the equivalent plastic strain rate inside the imperfection band is prescribed as a constant value of 1 throughout the loading:

$$\dot{\bar{\varepsilon}}^{p^B} - 1 = 0 . \tag{25}$$

The evolution equations for the geometric imperfection factor and the imperfection band angle are expressed in incremental forms as:

$$z_{t+1} = z_t \exp(\Delta t(\dot{\varepsilon}_{33}^B - \dot{\varepsilon}_{33}^H)) , \tag{26}$$

and

$$\tan(\beta_{t+1}) = \tan(\beta_t)\exp(\Delta t(1-\rho)\dot{\varepsilon}_{11}^H) . \tag{27}$$

In this section, subscripts t and $t+1$ denote the values of the corresponding variables at the beginning and at the end of the loading increment, respectively. The unit vector $\boldsymbol{n}_{t+1}$ lies normal to the imperfection band and its components can be updated as:

$$\mathbf{n}_{t+1} = \left[\cos(\beta_{t+1}) \quad \sin(\beta_{t+1}) \quad 0\right]^T . \tag{28}$$

Considering the third component of the normal vector as zero and applying plane-stress conditions, the equilibrium equation stated in Eq. (22) can be expanded as:

$$\begin{aligned} &(z_{t+1}\Sigma_{11,t+1}^B - \Sigma_{11,t+1}^H)n_{1,t+1} + (z_{t+1}\Sigma_{12,t+1}^B - \Sigma_{12,t+1}^H)n_{2,t+1} = 0, \\ &(z_{t+1}\Sigma_{21,t+1}^B - \Sigma_{21,t+1}^H)n_{1,t+1} + (z_{t+1}\Sigma_{22,t+1}^B - \Sigma_{22,t+1}^H)n_{2,t+1} = 0. \end{aligned} \tag{29}$$

The non-linear system of three scalar equations obtained by combining Eqs. (29) and (25) is expressed as:

$$\begin{aligned} R_1(\dot{\varepsilon}_{11}^H, \dot{c}_1, \dot{c}_2) &= (z_{t+1}\Sigma_{11,t+1}^B - \Sigma_{11,t+1}^H)n_{1,t+1} + (z_{t+1}\Sigma_{12,t+1}^B - \Sigma_{12,t+1}^H)n_{2,t+1} = 0, \\ R_2(\dot{\varepsilon}_{11}^H, \dot{c}_1, \dot{c}_2) &= (z_{t+1}\Sigma_{21,t+1}^B - \Sigma_{21,t+1}^H)n_{1,t+1} + (z_{n+1}\Sigma_{22,t+1}^B - \Sigma_{22,t+1}^H)n_{2,t+1} = 0, \\ R_3(\dot{\varepsilon}_{11}^H, \dot{c}_1, \dot{c}_2) &= \frac{\left[(\bar{\varepsilon}^{p^B})_{t+1} - (\bar{\varepsilon}^{p^B})_t\right]}{\Delta t} - 1 = 0. \end{aligned} \tag{30}$$

The above system of equations has been solved iteratively for each loading increment to determine the three independent unknown variables, i.e., $\dot{\varepsilon}_{11}^{H}$, $\dot{c}_1$ and $\dot{c}_2$. The internal state variables involved in the GLD-YLD coupled constitutive model can be expressed in the form of a general differential equation as:

$$\dot{\mathbf{y}} = \boldsymbol{g}_y(\mathbf{y}) . \tag{31}$$

In the above equation, vector $\mathbf{y}$ represents all the internal state variables of the GLD-YLD coupled constitutive model, which need to be updated using an explicit time integration scheme at the end of each loading increment. Further details on the numerical implementation of M–K imperfection approach are discussed in [67], where the procedure is illustrated in the form of a flow diagram. In that study, M–K approach was coupled with the GTN damage model, incorporating damage-based imperfections. The explicit time integration scheme for the internal variables of the GTN damage model was adopted from the work of Mansouri et al. [68].

In the present work, the coupling of M–K approach with the GLD model follows a similar framework. However, since several geometric parameters are involved in the GLD model, the integration scheme requires computation of several partial derivatives of these geometric parameters with respect to three internal variables, i.e., f, S and $\bar{\sigma}$ (e.g., $\partial C/\partial f$, $\partial C/\partial S$, $\partial e_1/\partial S$, $\partial g/\partial S$, $\partial g/\partial f$, $\partial \kappa/\partial f$, $\partial q/\partial f$ and $\partial \Sigma_h/\partial f$, etc.). These intermediate geometric parameters are also interrelated, as detailed in Appendix A and Appendix B.

In order to efficiently compute these complex and interdependent partial derivatives, while preserving the straightforward explicit integration schemes used in the GTN-M–K coupling [67], all geometric parameters are first defined symbolically in MATLAB. A built-in operator is then employed to calculate the explicit expressions for the required partial derivatives. This symbolic differentiation is performed only once, and the resulting explicit expressions are subsequently embedded into the main MATLAB program for practical use. This approach enables the real-time evaluation of the partial derivatives based on the actual values of the internal variables during plastic deformation.

The developed numerical tool based on the GLD model is validated in the next section through comparison with the GTN model predictions under uniaxial tension. The simulation runtimes for the GLD model under uniaxial tension, corresponding to void aspect ratios of 0.5, 0.999, 1.001, and 16 are approximately 8.5, 8.4, 4.3, and 7.7 minutes, respectively. The corresponding runtime for the conventional GTN model is less than one minute. These simulations were performed on an Intel Core i5, 6th generation, 2.4 GHz processor with 8 GB RAM. The resulting stress–strain responses are presented in Fig. 2. It is noteworthy that the simulation runtime for oblate voids is longer than that for

prolate voids. The reason being that the geometric equations for oblate voids are more complex than for prolate voids (see Appendix A and Appendix B). Overall, the simulation runtime for GLD model is much longer than for GTN model, due to the inclusion of an additional internal variable, namely the void aspect ratio.

In coupling the constitutive model with the M–K approach, the overall simulation runtime until the onset of localized necking increases significantly. To determine the three independent unknown variables (i.e., $\dot{\varepsilon}_{11}^{H}$, $\dot{c}_1$ and $\dot{c}_2$), the equilibrium equation Eq. (30) is numerically solved. This requires evaluating all state variables, particularly the stress and strain tensors, for both the homogeneous zone and the imperfection band. Consequently, the constitutive calculations are performed twice: once for the homogeneous zone and once for the imperfection band. After obtaining the three unknown variables, the internal variables are updated for both zones, resulting in a total of four constitutive calculations per M–K approach implementation. In addition, these calculations are repeated for 45 variations of initial imperfection band orientation (β_0), with the angle incremented by 2° from 0° to 90°. The minimum localization strain across all band orientations is then taken as the formability limit strain. This procedure significantly increases the simulation runtime compared to simple mechanical response simulations (see, e.g., Fig. 2). For instance, under the same computational setup described earlier, evaluating the formability limit of 2090-T3 aluminum alloy with a void aspect ratio *w*=16, an initial imperfection factor of $z_0 = 0.995$, and under balanced biaxial loading $(\rho = 1)$, requires approximatively 48 minutes for an initial band orientation of $\beta_0 = 0^\circ$. Consequently, computing all orientations results in a total runtime of around 36 hours. However, it has been well established in the literature that under balanced biaxial tension and plane-strain tension, the minimum localization strain occurs at $\beta_0 = 0^\circ$. Therefore, calculations for other orientations can be omitted to reduce computational cost. Similarly, in uniaxial tension, after a few test simulations for a particular material, a narrow range of β_0 can be identified, where the minimum localization strain occurs. This range can be first determined using the computationally efficient Gurson model and subsequently applied within the GLD model framework for the same material across different void aspect ratios.

3. Model validation and material response

In this section, the validation of the newly developed numerical implementation of the GLD-YLD coupled constitutive model is conducted. For this purpose, the developed MATLAB program is validated for various void aspect ratios through comparisons with earlier contributions reported in the literature (see [94]). Moreover, the predicted results are also compared with the GTN damage model, thus highlighting the effect of void shape in comparison to the classical case of spherical voids. The material response for various void aspect ratios and material orientations is also studied to verify that the model accurately predicts material behavior. This section discusses the following key points: an

assessment against the conventional GTN model, a comparison of the present numerical implementation with the results reported in [94], an analysis of material response at 0° and 90° loading orientation for the GLD model, validation of the numerical implementation of the YLD-2004-18p anisotropic model and finally, the material response with the combined GLD-YLD model.

3.1. Comparison with the GTN model

In this subsection, the results obtained using the developed MATLAB program for the GLD model are compared with the corresponding results obtained with the conventional GTN model under uniaxial tensile loading. Note that for comparison and validation purposes, the void shape evolution in the GLD model is deactivated. However, the initial void aspect ratio is varied (i.e., 0.5, 0.999, 1.001, and 16). The elasticity, isotropic hardening and GTN damage parameters used in the simulations are taken from [67] The corresponding stress–strain curves are presented in Fig. 2. This figure indicates that the uniaxial stress–strain response obtained with the GLD model coincides with that given by the conventional GTN model when the void aspect ratio is w = 0.999 or w = 1.001. These results are consistent with the formulation of the GLD model and provide a preliminary validation of the present numerical implementation when the aspect ratio approaches unity. However, it is important to note that the GLD model response does not correspond to that yielded by the GTN model when the void shape evolution is allowed during loading, even when the aspect ratio is unity. Note also that, with the GLD model, the material response is sensitive to the void aspect ratio w. More specifically, it can be seen that for prolate voids (i.e., w>1), the stress level is higher than that for oblate voids (i.e., w<1), which is also consistent with the GLD model and its porosity evolution.

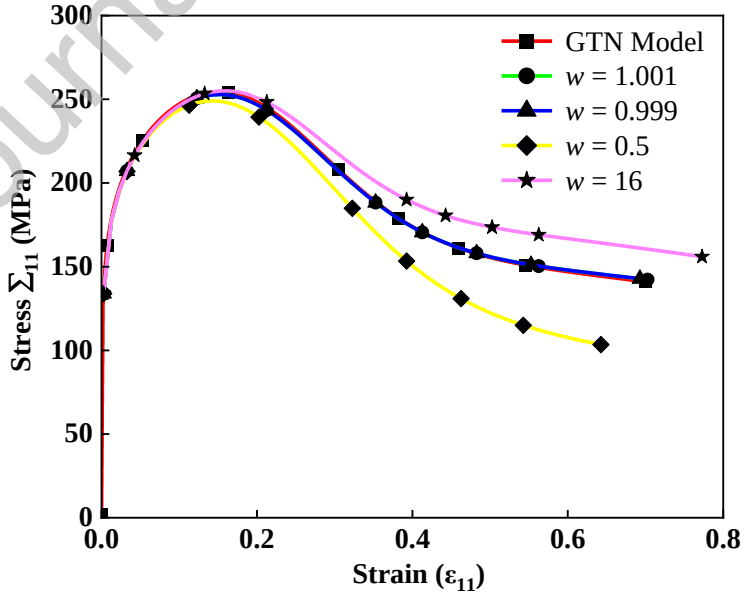

Fig. 2. Uniaxial stress–strain responses of the GLD model for several void aspect ratios and comparison with the conventional GTN model.

3.2. *Comparison with Benzerga [94] model*

The MATLAB-based program developed in this work is further validated by comparing its results with the work of Benzerga [94]. The loading conditions and material parameters have been taken identical to those presented in [94]. Fig. 3 depicts the results of model validation at various stress triaxialities and initial void aspect ratios. All the results indicate a similar response from both models, which validate the performance and accuracy of the developed MATLAB program.

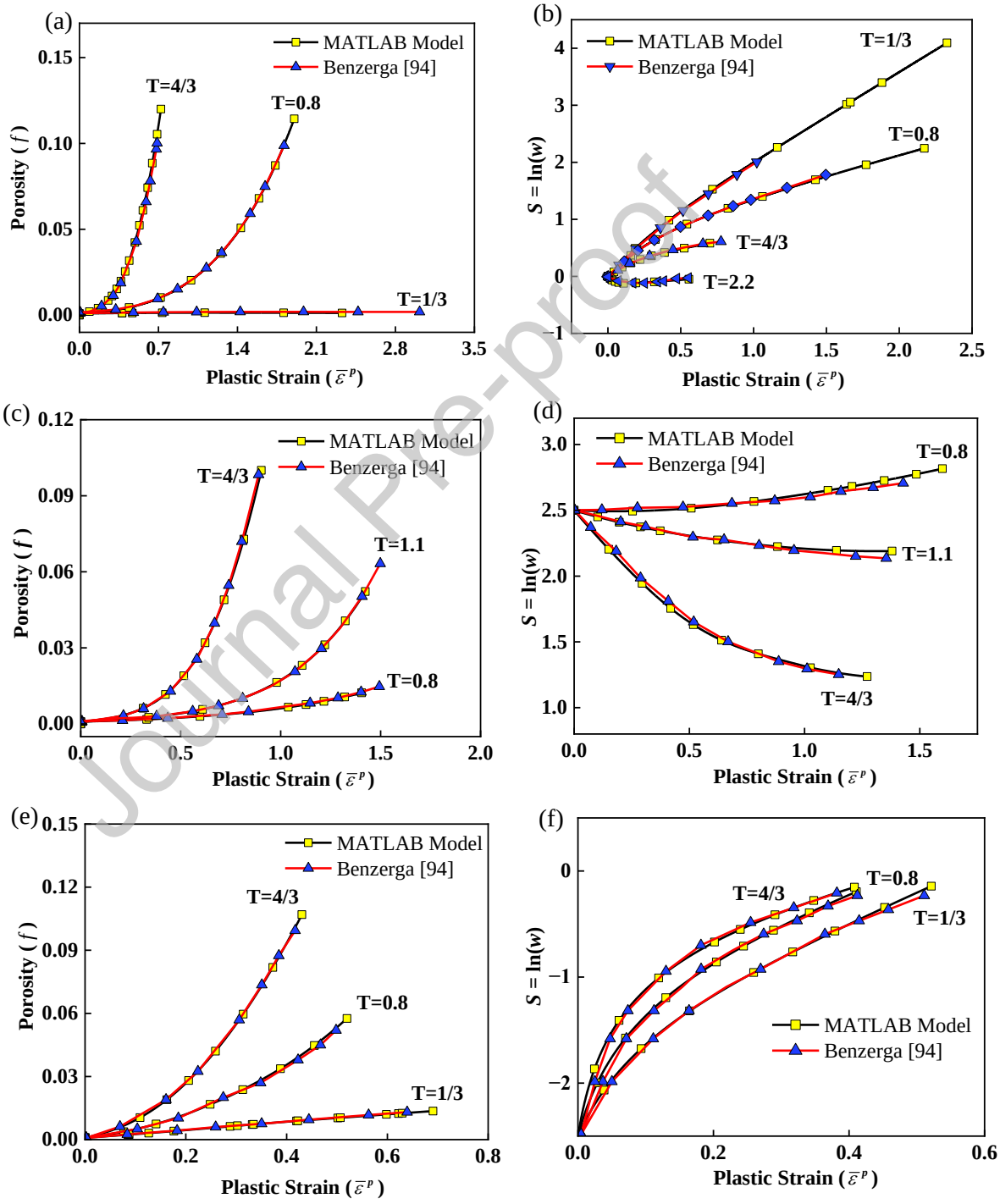

Fig. 3. Comparison of porosity and aspect ratio evolution between the present numerical implementation and Benzerga's reference curves [94], for various stress triaxiality ratios, with an initial porosity of f_0=0.0009 and an initial aspect ratio of (a, b) $S_0=\ln(w_0)=\ln(1)=0$, (c, d) $S_0=\ln(w_0)=\ln(12.1824)=2.5$ and (e, f) $S_0=\ln(w_0)=\ln(0.08208)=-2.50$.

3.3. Material response for the GLD model at 0^o void orientation

The validation of the developed model is further conducted here qualitatively by analyzing the material response at varying void aspect ratios and void orientations relative to the loading direction. The void orientation is schematically depicted in Fig. 4. It is noteworthy that the second-order tensor $\mathbf{X}$ involved in the GLD yield function (Eq. 1) governs the void orientation. Considering $\mathbf{X}=[-1/3 \quad 2/3 \quad -1/3 \quad 0 \quad 0 \quad 0]$ defines *y*-axis as the major axis of the ellipsoidal void. By contrast, the YLD-2004-18p anisotropic yield criterion assumes the *x*-axis as the rolling direction of the material. In the simplest case of the coupled GLD-YLD constitutive model, the relative angle between the ellipsoidal void major axis and the rolling direction of the anisotropic matrix material is considered $\gamma = 90^o$, as illustrated in Fig. 4. However, a more generalized case is examined in Section 5.1.3, where the rolling direction of the matrix material is misaligned with the void orientation (i.e., $\gamma \neq 90^o$). This approach better reflects real-world conditions and enhances the model applicability.

Uniaxial tensile loading is applied here along the X_1 axis, which is considered as the major loading direction. The void orientation angle θ is defined as the angle between the minor loading direction (i.e., X_2 axis) and the ellipsoidal void major axis (i.e., *y* axis, see Fig. 4). To investigate the effects of void orientation, the void and the rolling direction are fixed along the *x*–*y* coordinate axes, while the *x*–*y* system is rotated relative to the X_1–X_2 reference frame. This approach alters the void orientation, while keeping the loading direction constant along the X_1 axis.

Fig. 5 illustrates the effect of void aspect ratio on material response for void orientation $\theta = 0^o$. In Fig. 5 (a, b), only void growth mechanism is considered, which shows the highest ultimate tensile strength achieved when the void aspect ratio approaches 1. In addition, oblate voids (i.e., $w<1$) exhibit less ductility, while prolate voids (i.e., $w>1$) exhibit more ductility. Furthermore, since the uniaxial tension is applied along the X_1 axis, therefore, the void aspect ratio decreases with the increase of strain when $\theta = 0^o$, as shown in Fig. 5b.

In Fig. 5 (c, d), both of the void growth and void nucleation mechanisms are considered. Note that in the current constitutive framework, the strain-controlled void nucleation model proposed by Chu and Needleman [6] is considered, which is based on a statistical approach. For this nucleation model, the porosity evolution owing to nucleation follows uniform distribution, and for a certain strain range, the porosity evolution due to void nucleation is maximum. Fig. 5c shows the stress–strain responses, where it can be observed that, unlike the previous case illustrated in Fig. 5a, both the ultimate tensile strength

and ductility increase as the void aspect ratio increases from 0.5 to 16. Fig. 5d displays the corresponding evolution of void shape, which follows the same trend as that of the previous case (see Fig. 5b).

Fig. 5(e, f) reports the stress–strain response of the material by using the GLD model with consideration of all of the void evolution mechanisms (i.e., growth, nucleation and coalescence). With the inclusion of all these mechanisms, a more realistic material response is predicted (see Fig. 5e, as compared to Figs. 5c and 5a). The results reported in Fig. 5e also reveal that both the material strength and ductility for prolate voids are higher as compared to oblate void shapes.

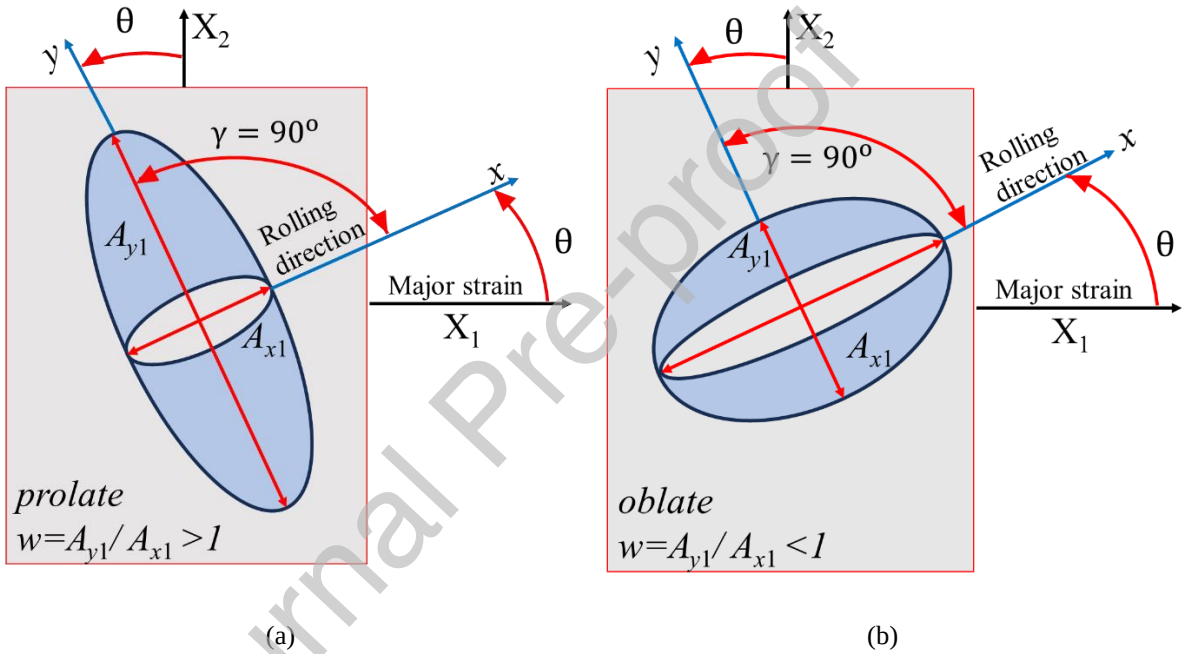

Fig. 4. Illustration of void orientation, matrix material rolling direction, and major strain loading direction. Uniaxial tension is applied along the X_1 axis, while the void *y* axis is oriented at an angle θ with respect to X_2 axis for: (a) prolate voids, and (b) oblate voids.

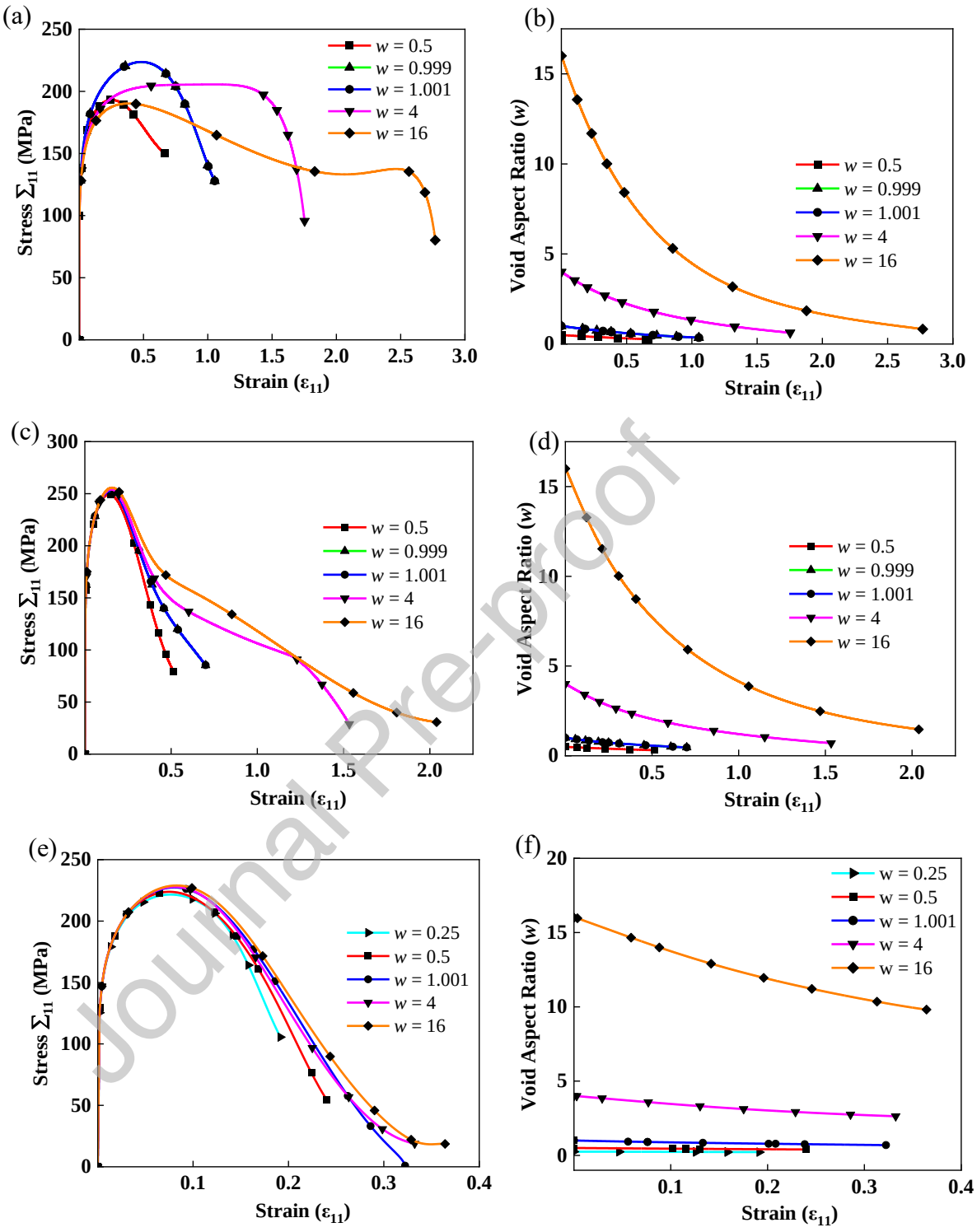

Fig. 5. Stress–strain responses (a, c, e) and evolution of void aspect ratio *w* (b, d, f), for void orientation $\theta = 0^{o}$ under uniaxial tension, obtained by the GLD model with (a, b) only void growth mechanism, (c, d) void growth and nucleation mechanisms and (e, f) void growth, nucleation and coalescence mechanisms plotted at different initial void aspect ratios.

3.4. Material response for the GLD model at 90^{o} *void orientation*

To illustrate the inherent anisotropic nature of the GLD model, voids are now oriented at 90^{o} (see Fig. 4). Note that, similar to the previous case, the uniaxial tension is applied along the X_1 axis. The stress–strain responses and void shape evolution curves for this configuration are presented in Fig. 6 for the three cases: only void growth mechanism; void growth and nucleation mechanisms; and finally, void growth, nucleation and coalescence mechanisms, respectively. From these results, and comparing them with the previous outcomes at 0° loading orientation, it can be concluded that the prolate voids exhibit higher material strength and ductility, as compared to oblate voids for both 0^{o} and 90^{o} orientation. However, since the void orientation is now orthogonal to the uniaxial tensile loading direction (applied along axis X_1), therefore, the void aspect ratio increases with the strain, as shown in Fig. 6(a, b), Fig. 6(c, d), and Fig. 6(e, f), which is fully consistent with the orientation of the void with respect to the loading direction. Also, similar to the previous case of 0° loading orientation, it clearly appears that with the inclusion of all three mechanisms of void growth, nucleation and coalescence, a more realistic material response is predicted (see Fig. 6e, as compared to Figs. 6c and 6a).

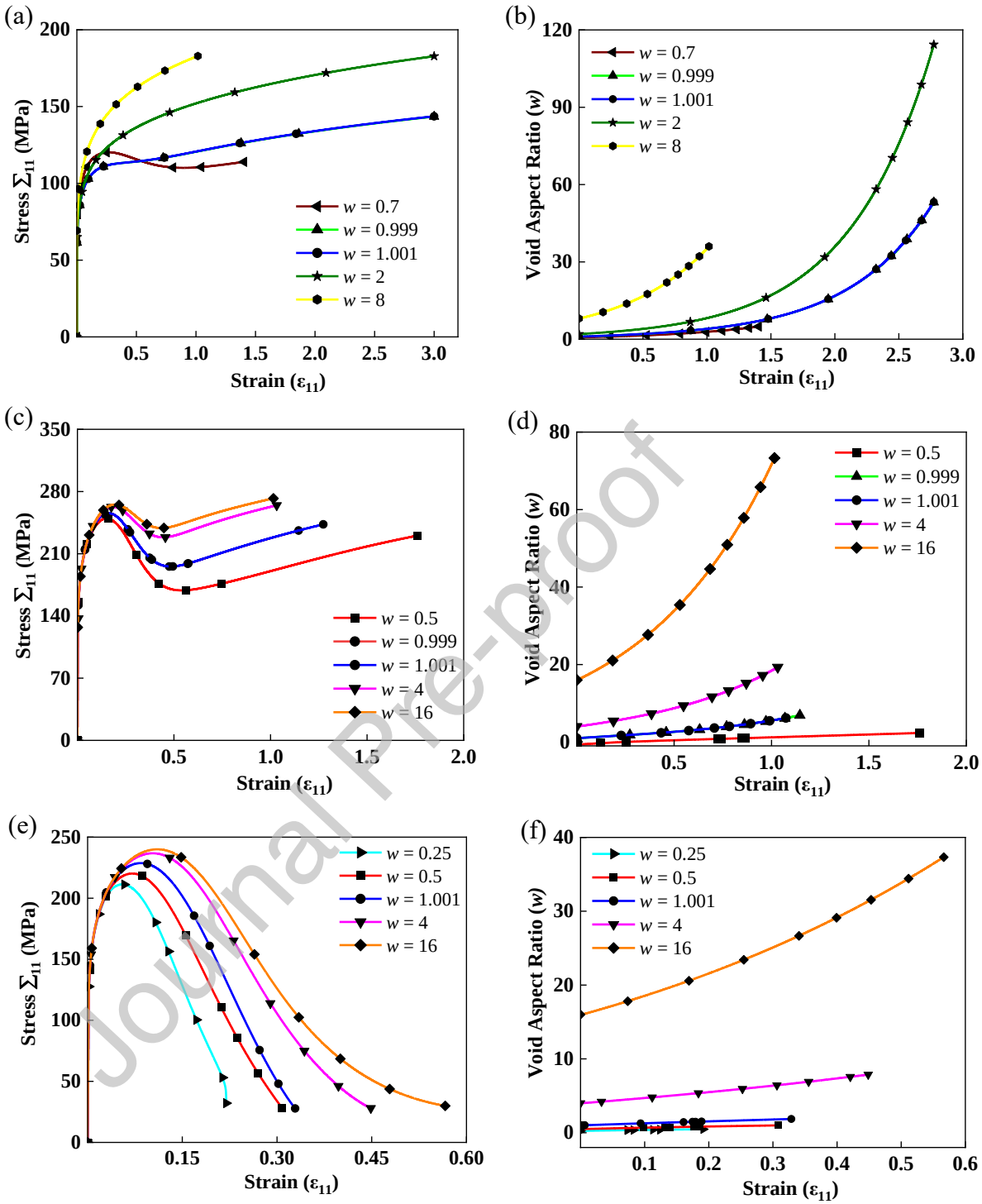

Fig. 6. Stress–strain responses (a, c, e) and evolution of void aspect ratio *w* (b, d, f), for void orientation $\theta = 90^{o}$ under uniaxial tension, obtained by the GLD model with (a, b) only void growth mechanism, (c, d) void growth and nucleation mechanisms and (e, f) void growth, nucleation and coalescence mechanisms plotted at different initial void aspect ratios.

3.5. *YLD anisotropic yield surface verification*

In this subsection, the numerical implementation of the YLD-2004-18p anisotropic yield function is validated. For this purpose, the GLD model was deactivated in the MATLAB program to evaluate the performance of the YLD-2004-18p model. The elastic–plastic material parameters as well as the reference data (i.e., yield locus curve, normalized *r*-values, and normalized stress values) are taken from the work of Barlat et al. [42]. These results are presented in Fig. 7. The consistency of the reproduced values with reference data confirms the accurate implementation of the YLD-2004-18p anisotropic yield function within the MATLAB code.

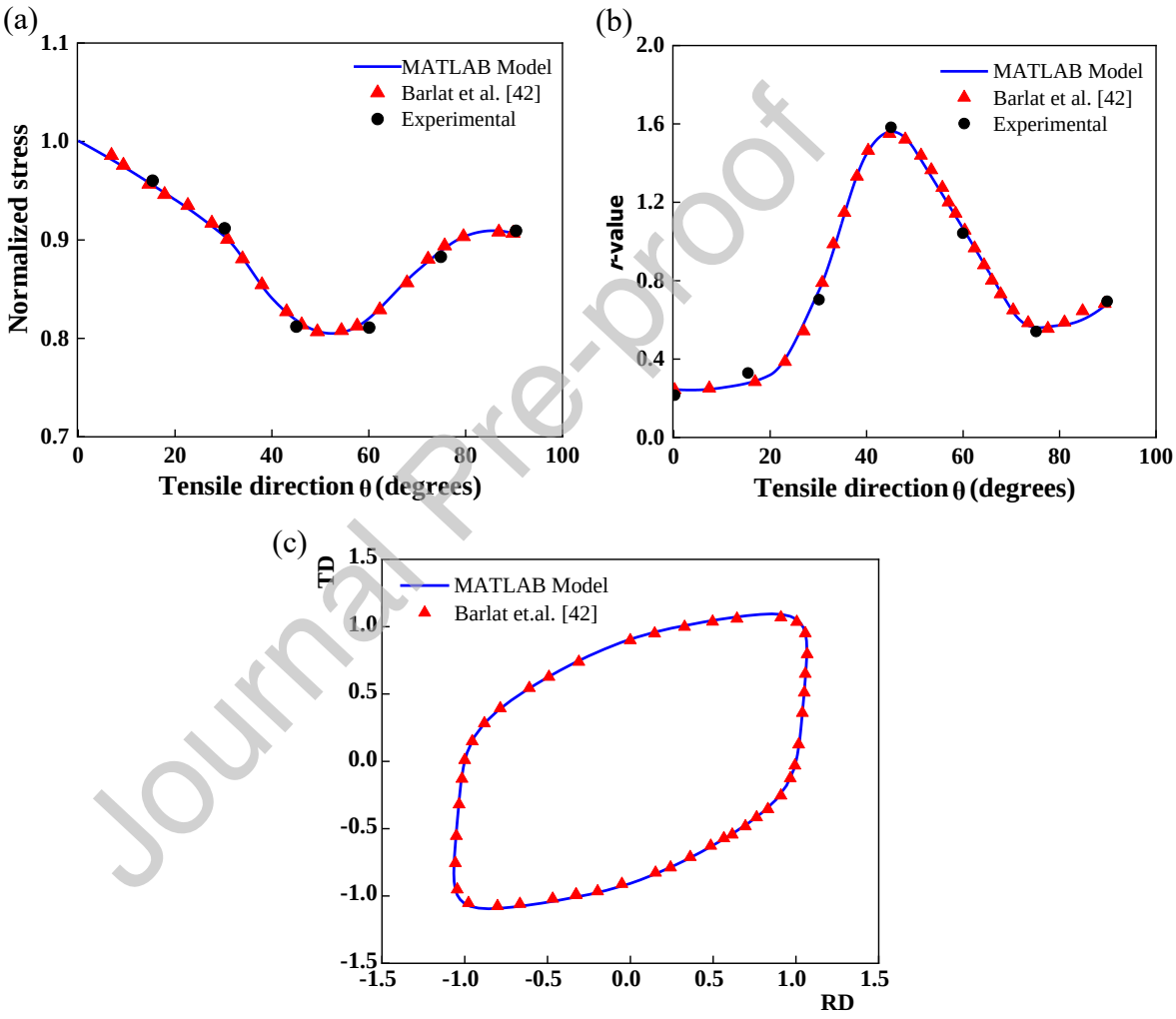

Fig. 7. Validation of the numerical implementation of the YLD-2004-18p anisotropic yield function in MATLAB by comparison with the reference data taken from Barlat et al. [42] for: (a) normalized stress curve, (b) *r*-value curve, and (c) yield locus curve in rolling direction (RD) and transverse direction (TD) plane. The material considered is an aluminum alloy 2090-T3.

3.6. Material response using the GLD model coupled with the YLD anisotropic yield function

In the present constitutive modeling, anisotropy arises from two key phenomena: first, the dense matrix material of the RVE exhibits non-quadratic anisotropic behavior described by the YLD-2004-18p yield function, and second, the ellipsoidal void shape induces its own anisotropy. As a result, these factors result in highly complex material behavior, which necessitates a thorough investigation before predicting the FLD. For this purpose, the material response is investigated by plotting stress–strain curves under uniaxial tension for different void aspect ratios and material orientations. The material anisotropy parameters used in the simulations correspond to the aluminum alloy 2090-T3, and are the same as those used in the previous section.

First, in Fig. 8, stress–strain responses are presented under uniaxial tension for 0^{o}, 45^{o} and 90^{o} material orientation (i.e., angle between the rolling direction and the applied loading axis) using the YLD anisotropic model without considering damage. The results show that material hardening is strongly dependent on the material orientation. This directional dependence of material hardening response is attributed solely to the anisotropy of the dense matrix material. Due to this material anisotropy, the strain hardening at 0^{o} loading direction is more pronounced compared to 90^{o}, which in turn exceeds the strain hardening observed at 45^{o} loading direction.

Fig. 9 presents the stress–strain responses under uniaxial tension along 0^{o}, 45^{o} and 90^{o} void orientations using the GLD model without matrix-induced anisotropy for three values of void aspect ratio, i.e., 0.25, 1.001 and 16. Unlike Fig. 8, where matrix-induced anisotropy affects the strain hardening behavior, Fig. 9 highlights the isolated effect of damage-induced anisotropy. This anisotropic behavior originates from the consideration of ellipsoidal void shape in the constitutive model. From Fig. 9, it is evident that the softening rate is greater in the 0^{o} void orientation compared to 90^{o} for prolate void shapes. Conversely, for oblate voids, the softening rate in the 90^{o} void orientation exceeds that of the 0^{o} void orientation.

Finally, both sources of anisotropy are integrated into the GLD-YLD coupled model. The corresponding stress–strain responses under uniaxial tension along 0^{o}, 45^{o} and 90^{o} void orientations are presented in Fig. 10 for three void aspect ratios: 0.25, 1.001, and 16. It is important to note that, in the GLD-YLD coupled model, the void orientation is assumed to be aligned with the rolling direction of the matrix material for simplicity. From this Fig. 10, it is evident that the anisotropic material behavior is exhibited throughout the stress–strain response. In the positive hardening regime, the YLD-induced anisotropy dominates, while in the softening regime, beyond ultimate tensile strength, damage-induced anisotropy becomes more significant.

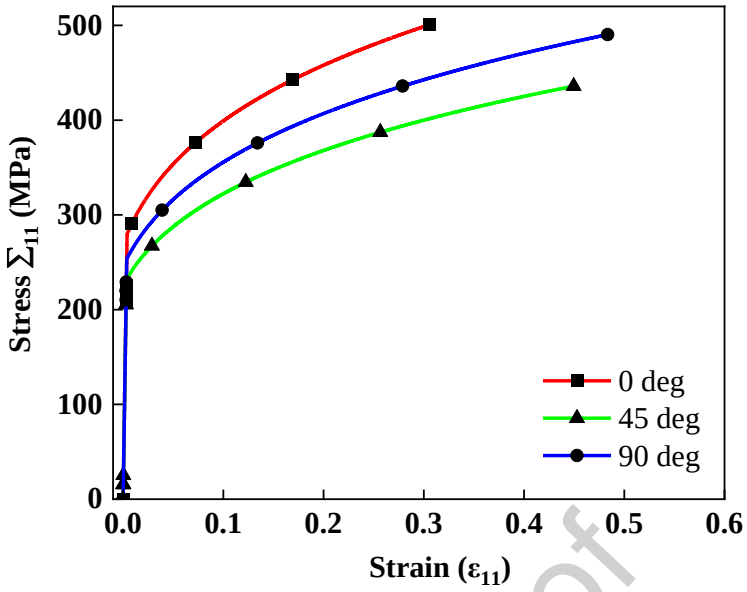

Fig. 8. Stress–strain responses under uniaxial tension along 0°, 45° and 90° orientations for the YLD anisotropic model without damage.

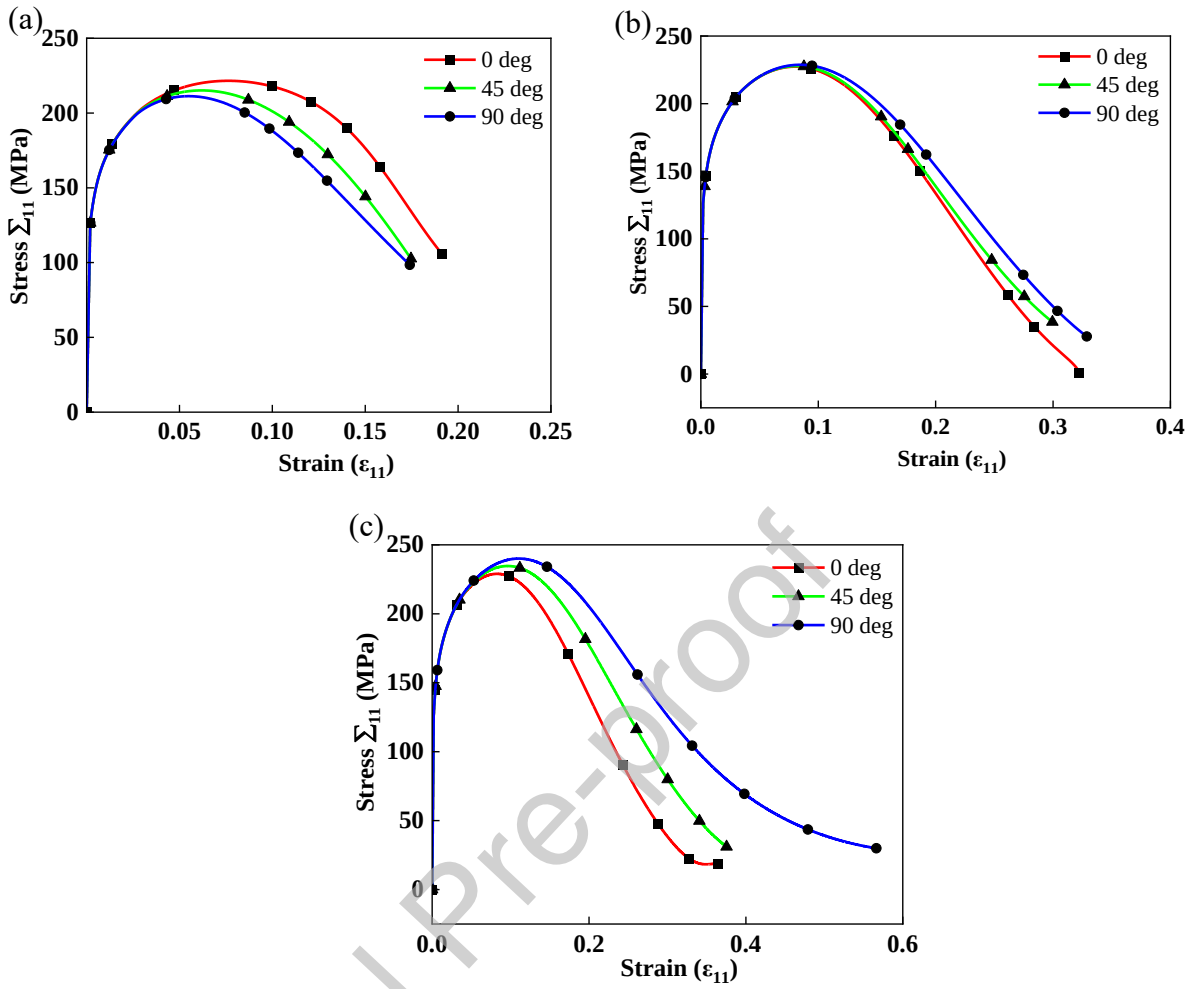

Fig. 9. Stress–strain responses under uniaxial tension along 0^{o}, 45^{o} and 90^{o} void orientations for the GLD model without matrix-induced anisotropy: (a) w = 0.25, (b) w = 1.001, and (c) w = 16.

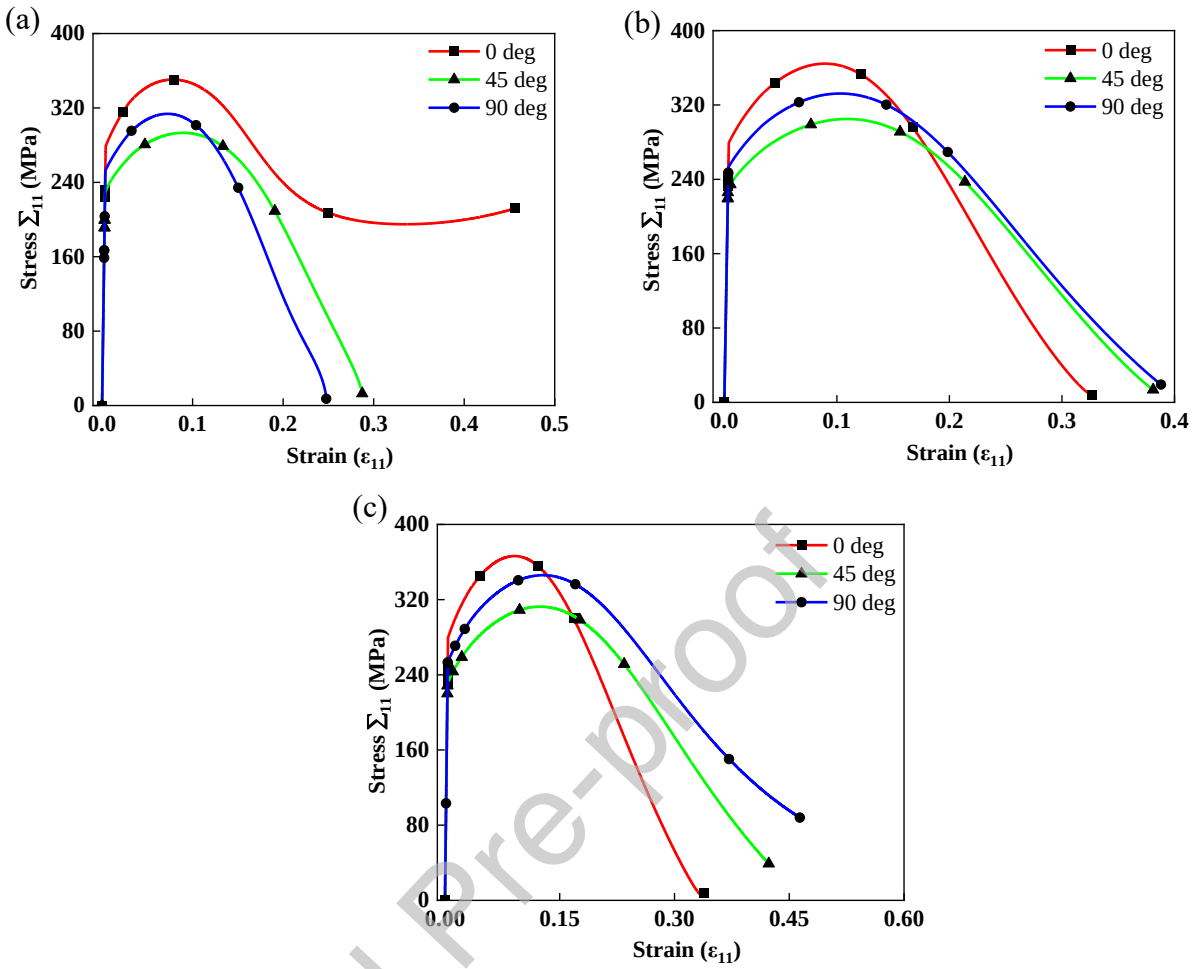

Fig. 10. Stress–strain responses under uniaxial tension along 0°, 45° and 90° void orientations for the GLD-YLD coupled model: (a) w = 0.25, (b) w = 1.001, and (c) w = 16.

4. Material parameters

In this study, material parameters corresponding to strong damage have been considered in order to emphasize the high impact of void shape on the material response. These sets of elastic–plastic and damage material parameters have been reported in [67] and are listed in Table 1.

Table 1

Elasticity, isotropic hardening and damage parameters used in the simulations.

E (GPa)	υ	K (MPa)	ε_0	n	f_0	f_{cr}	δ_{GTN}
70	0.3	646	0.025	0.227	0.001	0.00213	5
q_1	q_2	q_3	ψ	s_N	ε_N		
1.5	1	2.15	0.27	0.1	0.27		

In order to investigate and compare the impact of void shape on the FLDs for different anisotropic materials, three types of anisotropic aluminum materials, i.e., 6111-T4 (weak anisotropy), 2090-T3 (medium anisotropy), and FM-08 (strong anisotropy) along with isotropic materials have been coupled with the GLD-based damage model. The corresponding material anisotropy parameters are reported in Table 2 [42,95]. To investigate the relative measure of anisotropy exhibited by these three types of materials, the corresponding *r*-values and normalized yield strength values are calculated for different material orientations. The material orientation is defined here as the angle between the major loading direction X_1 and the rolling direction. The predicted results are presented in Fig. 11. When the material orientation is varied from 0° to 90°, the variations in *r*-values and normalized yield strength for 6111-T4 aluminum alloy are relatively small as compared to 2090-T3 and FM-08 aluminum alloys. It is also worth noting that one peak in the *r*-value curve is depicted for the 2090-T3 aluminum alloy, as compared to the FM-08 aluminum alloy for which two peaks are observed. Moreover, it has been shown in [95] that, in deep drawing process, six ears are observed for the 2090-T3 aluminum alloy, as compared to eight ears for the FM-08 aluminum material. Therefore, investigating these three types of aluminum alloys encompasses a wide range of anisotropic materials, ranging from weakly anisotropic to strongly anisotropic.

Table 2

YLD-2004-18p material parameters for 6111-T4 (weak anisotropy), 2090-T3 (medium anisotropy), and FM-08 (strong anisotropy) aluminum materials (exponent a = 8).

	Material anisotropy parameters		
	Weak anisotropy (6111-T4)	**Medium anisotropy (2090-T3)**	**Strong anisotropy (FM-08)**
c'_{12}	1.241024	-0.06988	0.7297
c'_{13}	1.078271	0.936408	0.8777
c'_{21}	1.216463	0.079143	0.4252
c'_{23}	1.223867	1.00306	0.7268
c'_{31}	1.093105	0.524741	1.1386
c'_{32}	0.889161	1.36318	1
c'_{44}	1.349094	0.954322	1.3485
c'_{55}	0.557173	1.06906	1
c'_{66}	0.501909	1.02377	1
c''_{12}	0.775366	0.981171	1.0513
c''_{13}	0.922743	0.476741	1.0389
c''_{21}	0.765487	0.575316	1.3289

c''_{23}	0.793356	0.866827	1.1775
c''_{31}	0.918689	1.14501	0.7651
c''_{32}	1.027625	-0.079294	0.9169
c''_{44}	0.589787	1.40462	0.0432
c''_{55}	1.112273	1.1471	1
c''_{66}	1.115833	1.05166	1

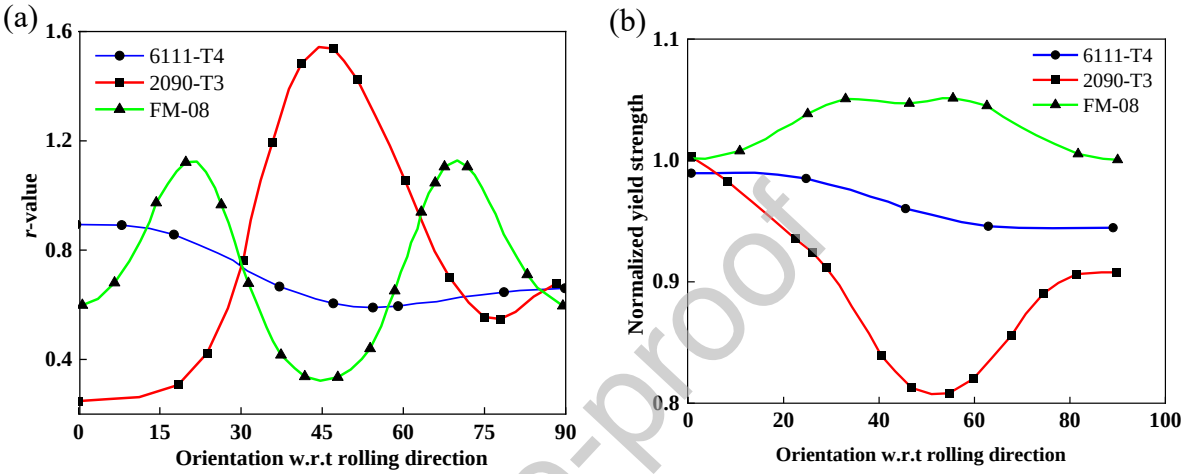

Fig. 11. Plots for the evolution of: (a) *r*-value, and (b) normalized yield strength, for 6111-T4 (weak anisotropy), 2090-T3 (medium anisotropy), and FM-08 (strong anisotropy) aluminum materials.

Lastly, FLDs of two real materials, i.e., 6111-T4 and 2090-T3 aluminum alloys, have also been predicted with the GLD-YLD coupled model. To this end, the corresponding material parameters are listed in Table 3 [96,97] for 6111-T4 aluminum alloy. For 2090-T3 aluminum alloy, the material parameters are calibrated according to undamaged constitutive model in the existing literature [98]. The material anisotropy parameters have already been reported in Table 2. The predicted results are presented in the next section.

Table 3

Elasticity, hardening and damage parameters for the 6111-T4 aluminum material.

E (GPa)	υ	K (MPa)	ε_0	n	f_0	f_{cr}	δ_{GTN}
70.5	0.342	750	0.02	0.2	0	0.15	4
q_1	q_2	q_3	ψ	s_N	ε_N		
1.5	1	2.25	0.04	0.1	0.3		

5. Results and discussions

This study primarily focuses on the investigation of the effects of void shape, void orientation, material anisotropy, material damage, isotropic hardening, and relative angle between void orientation and matrix material rolling direction on the prediction of FLDs. This section is divided into four subsections. For the first subsection, a fictitious material exhibiting strong damage has been purposely considered to highlight the impact of void shape. As to the material anisotropy parameters considered in this subsection, they correspond to the previously-discussed three types of anisotropic materials (namely, 6111-T4, 2090-T3, and FM-08 aluminum alloys). The second and third subsections discuss the FLD prediction for two real materials, i.e., 6111-T4 and 2090-T3 aluminum alloys, and the predicted results are compared with experimental data taken from [99] and [100], respectively. The fourth subsection finally discusses the effect of isotropic hardening parameters, void shape, and void orientation on the FLD prediction of a material exhibiting strong damage and strong anisotropy.

5.1. Void shape and void orientation effects on the prediction of FLDs

5.1.1 Case of weak anisotropy material

The coupled GLD-YLD constitutive model is applied here, in conjunction with the M–K localized necking approach, for the prediction of FLDs for a weakly anisotropic material. The material parameters (elasticity, hardening, anisotropy, and damage) corresponding to this material (i.e., 6111-T4) are summarized in Tables 2 and 3. The predicted FLDs are shown in Fig. 12a. From this figure, it can be observed that by increasing the void aspect ratio from 0.25 to 16 (i.e., varying void shape from oblate to prolate), the formability limit strains increase for all loading paths, i.e., from uniaxial tension to balanced biaxial tension. Since the present material model exhibits anisotropy originating from two separate phenomena, i.e., non-spherical void shape and dense matrix material anisotropy, therefore, the FLDs are also predicted for material orientations of 45° and 90° with respect to the major principal strain axis to investigate the true effect of material anisotropy on the FLDs. Here, the dense matrix material anisotropy is weak, hence the damage-induced anisotropy due to void shape is predominant. Fig. 12b and Fig. 12c show that at 45° and 90° material orientation, higher formability limit strains are obtained for higher values of void aspect ratio, except at balanced biaxial tension, where the formability limit strain for prolate voids (i.e., w=16) is less than that for spherical voids (w=1.001). This unusual response for balanced biaxial tension is likely attributable to void nucleation phenomenon. Indeed, since void nucleation rate is maximum at certain plastic strain range, it comes that for w=16 under balanced biaxial tension, damage-induced softening is promoted owing to more void nucleation, thus leading to earlier necking as compared to the case of spherical voids (w=1.001). However, this peculiar behavior observed for balanced biaxial tension loading path does not alter the overall trend valid for all other strain path ratios, namely, higher formability limit strains are obtained for prolate void shapes as compared to oblate voids.

In order to investigate the effect of material orientation on formability limit strains, Fig. 13 shows the evolution of the major strain with the material orientation under uniaxial tension (Fig. 13a, 13b), plane-strain tension (Fig. 13c, 13d), and balanced biaxial tension (Fig. 13e, 13f). Four constitutive models are considered in each of these figures. GTN-VM represents the conventional Gurson–Tvergaard–Needleman damage model without dense matrix material anisotropy and void shape anisotropy. GLD-VM represents the void shape dependent damage model without dense matrix material anisotropy. GTN-YLD represents the conventional GTN damage model coupled with dense matrix material anisotropy. Finally, GLD-YLD represents the complete model, which accounts for both damage-induced anisotropy and dense matrix material anisotropy. It is worth noting that in what follows, due to the symmetry of the predicted results, the latter are shown only for material orientation between 0° and 180°. Fig. 13(a, b) shows that, for uniaxial tension, the major strain for prolate void shape (i.e., w=16) is higher as compared to spherical and oblate voids (w=0.25). Moreover, with the change in material orientation for prolate voids, the maximum value of major strain is achieved for 90°, and the minimum value for 0° material orientation. As to the oblate voids, the maximum value of major strain is achieved for 0°, and the minimum value for 90° material orientation. A similar trend is observed for plane-strain tension as seen in Fig. 13(c, d). For balanced biaxial tension, the major strain for prolate voids is higher than that of oblate voids as expected. However, the major strain for spherical voids is higher than that of prolate voids, except near 0° material orientation. As previously discussed, this unusual higher formability limit for spherical voids as compared to prolate voids, for the particular case of balanced biaxial tension, is attributable to void nucleation phenomenon.

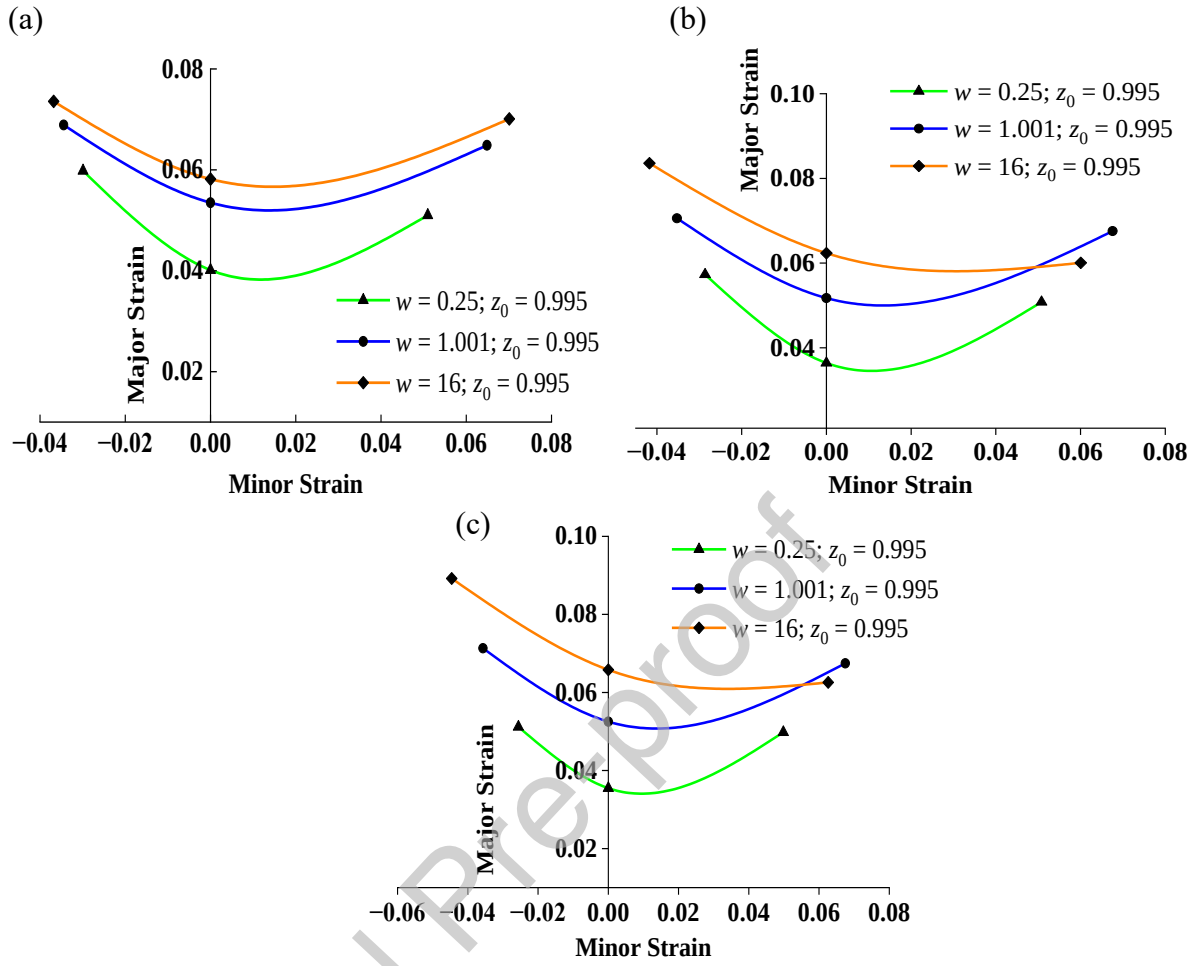

Fig. 12. FLDs for weak anisotropy material, for void aspect ratios of 0.25, 1.001, and 16, and at: (a) 0° material orientation, (b) 45° material orientation, and (c) 90° material orientation.

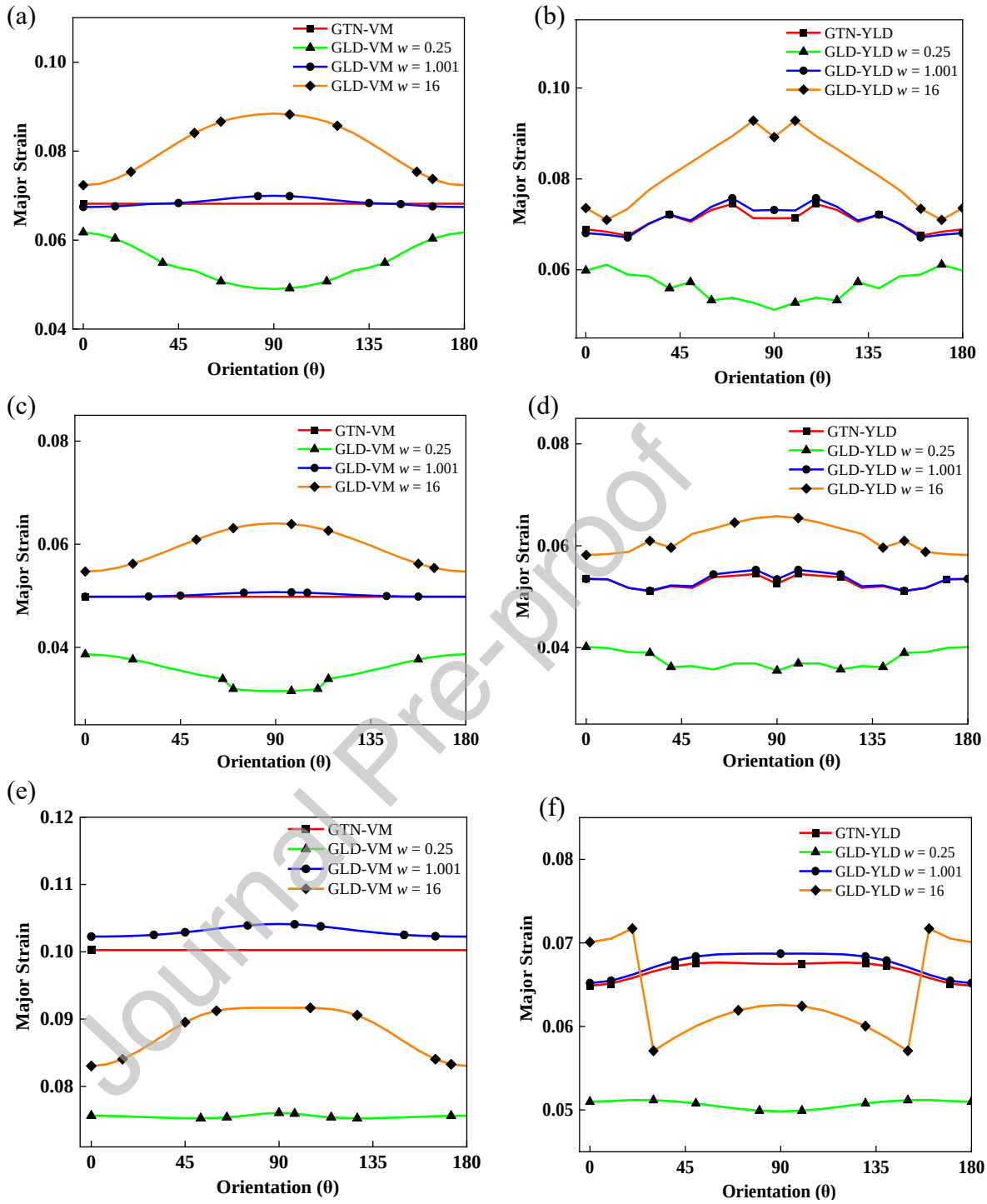

Fig. 13. Evolution of the major strain with respect to material orientation, for weak anisotropy material, for w=0.25, 1.001, and 16, and for: (a, b) uniaxial tension, (c, d) plane-strain tension, and (e, f) balanced biaxial tension.

5.1.2 Case of medium anisotropy material

The FLDs for a medium anisotropy material are investigated here for three void aspect ratios and three material orientations. The material parameters (elasticity, hardening, anisotropy, and damage)

corresponding to 2090-T3 aluminum alloy are listed in Tables 2 and 3. The results of the predicted FLDs are shown in Fig. 14. This latter figure depicts that the formability limit strains increase with the increase in void aspect ratio from 0.25 to 16. This upward shift of FLD is observed for all the material orientations and for all the loading paths. The results indicate that prolate, needle-like voids, exhibit higher formability as compared to oblate, plate-like flat voids. For further investigating the effect of material anisotropy on formability, the predicted major strains of the material for different void aspect ratios are presented in Fig. 15 for material orientations ranging from 0° to 180°, in the cases of uniaxial tension, plane-strain tension, and balanced biaxial tension. It is interesting to note from this Fig. 15 that the FLDs strongly depend on the material orientation. For uniaxial tension (see Fig. 15a), the highest formability limit strains are observed at 60° and 120° for all the void shapes. For plane-strain tension (see Fig. 15b), the highest formability limit strain is observed for 0° for both prolate and oblate voids, while at 90° for spherical voids. For balanced biaxial tension (see Fig. 15c), 90° material orientation corresponds to the highest formability limit strain for prolate voids, while the lowest for spherical and oblate voids. The results show that in the presence of non-spherical voids, the overall material formability is highly anisotropic in nature, and for accurate FLD prediction, both void shape and void orientation must be considered.

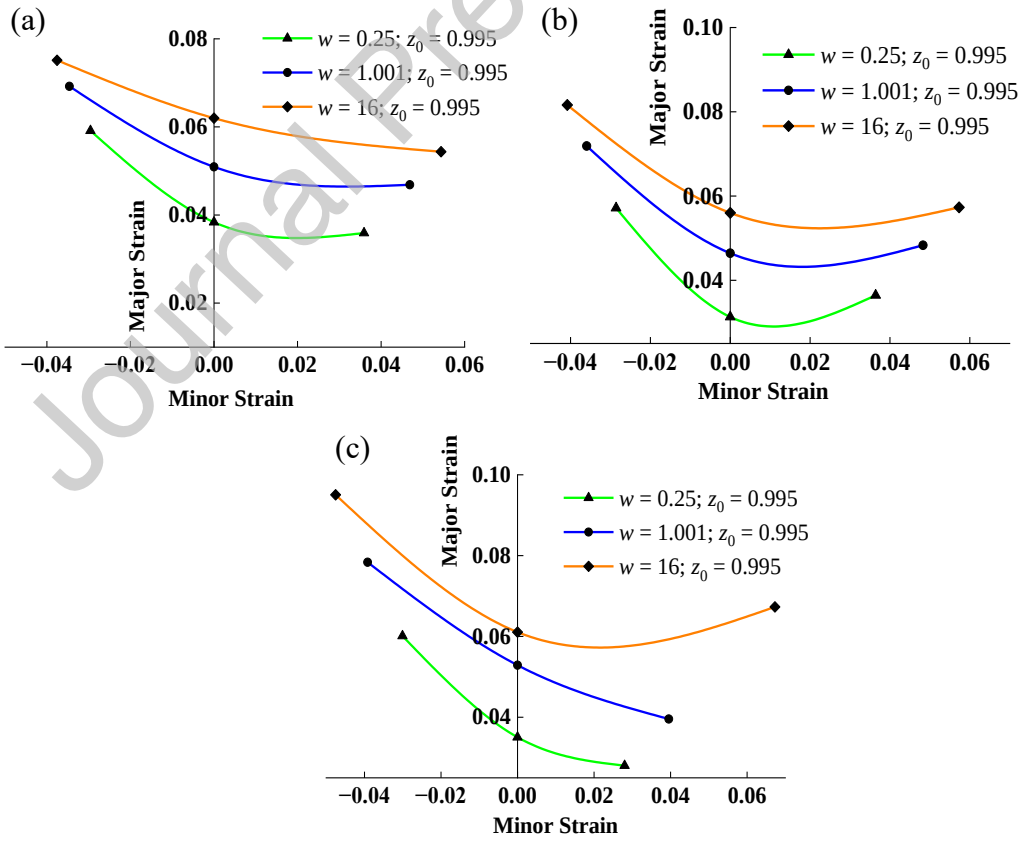

Fig. 14. FLDs for medium anisotropy material, for void aspect ratios of 0.25, 1.001, and 16, and at: (a) 0° material orientation, (b) 45° material orientation, and (c) 90° material orientation.

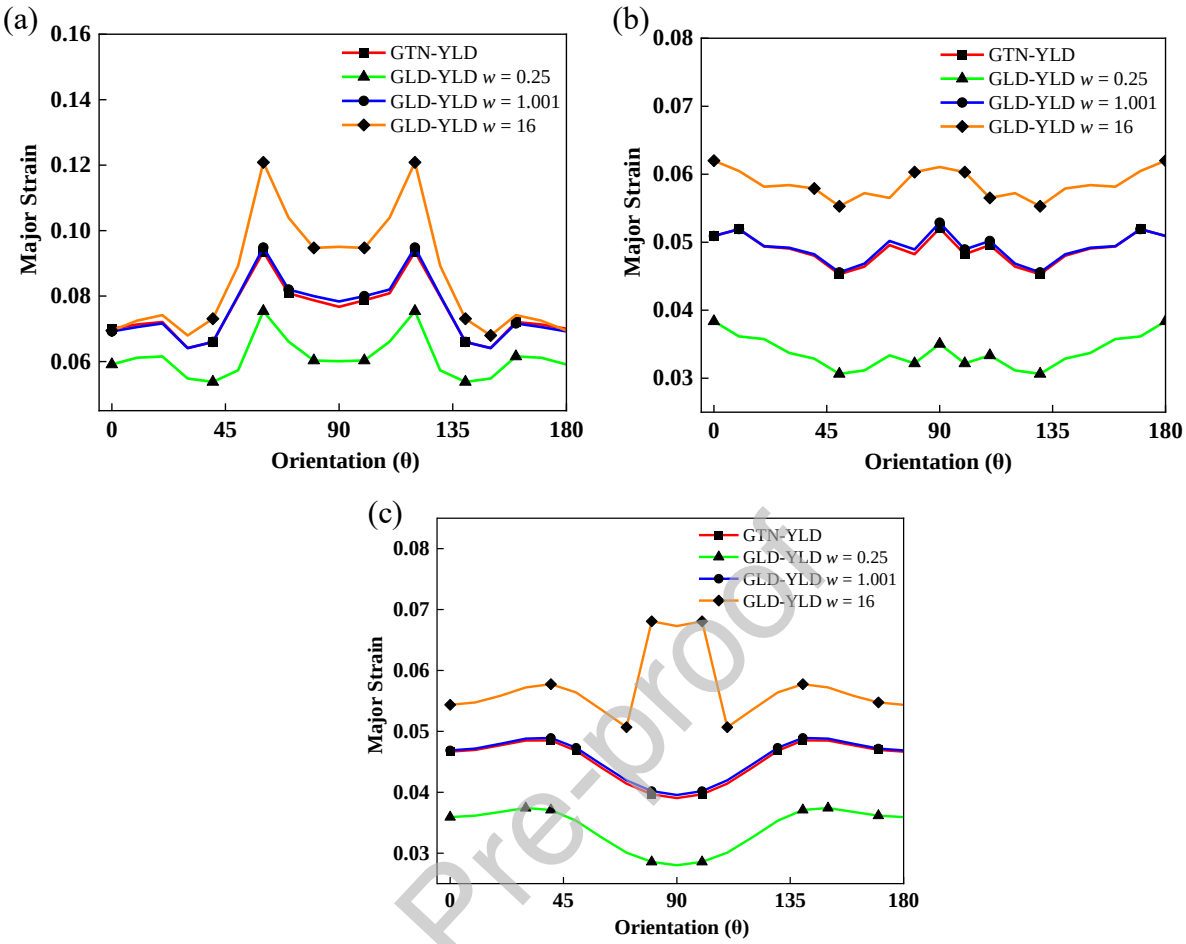

Fig. 15. Evolution of the major strain with respect to material orientation, for medium anisotropy material, for w=0.25, 1.001, and 16, and for: (a) uniaxial tension, (b) plane-strain tension, and (c) balanced biaxial tension.

5.1.3 Case of strong anisotropy material

The strong anisotropy aluminum alloy FM-08, whose material parameters are summarized in Tables 2 and 3, is considered here to investigate the effects of void shape and orientation on the predicted forming limit diagrams. Fig. 16 presents the FLDs for this aluminum alloy, at 0°, 45°, and 90° material orientations, while Fig. 17 provides the evolution of the major strain with the material orientation, for three particular loading paths. It can be observed that the forming limit strains are the lowest for oblate voids (i.e., w = 0.25), followed by spherical voids (i.e., w = 1), and then prolate voids (i.e., w = 16). These results highlight the pronounced anisotropic behavior of the material, resulting from the combined influence of two anisotropy-inducing factors, i.e., void shape and dense matrix material anisotropy.

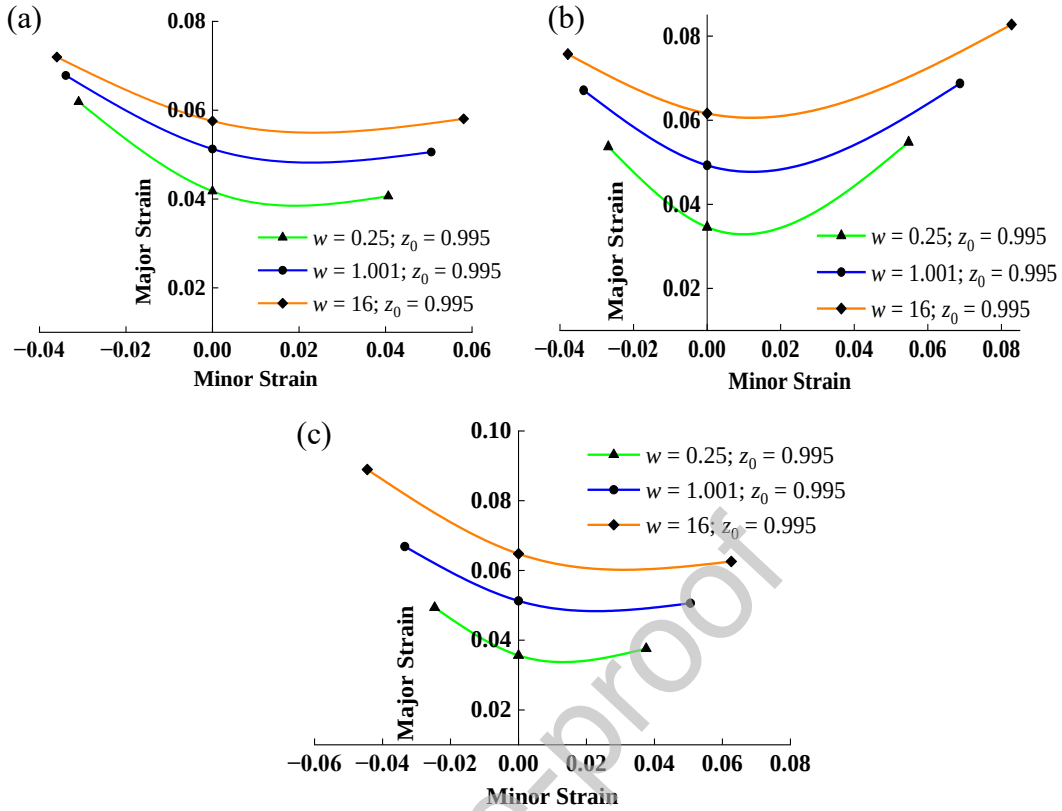

Fig. 16. FLDs for strong anisotropy material, for void aspect ratios of 0.25, 1.001, and 16, at: (a) 0° material orientation, (b) 45° material orientation, and (c) 90° material orientation.

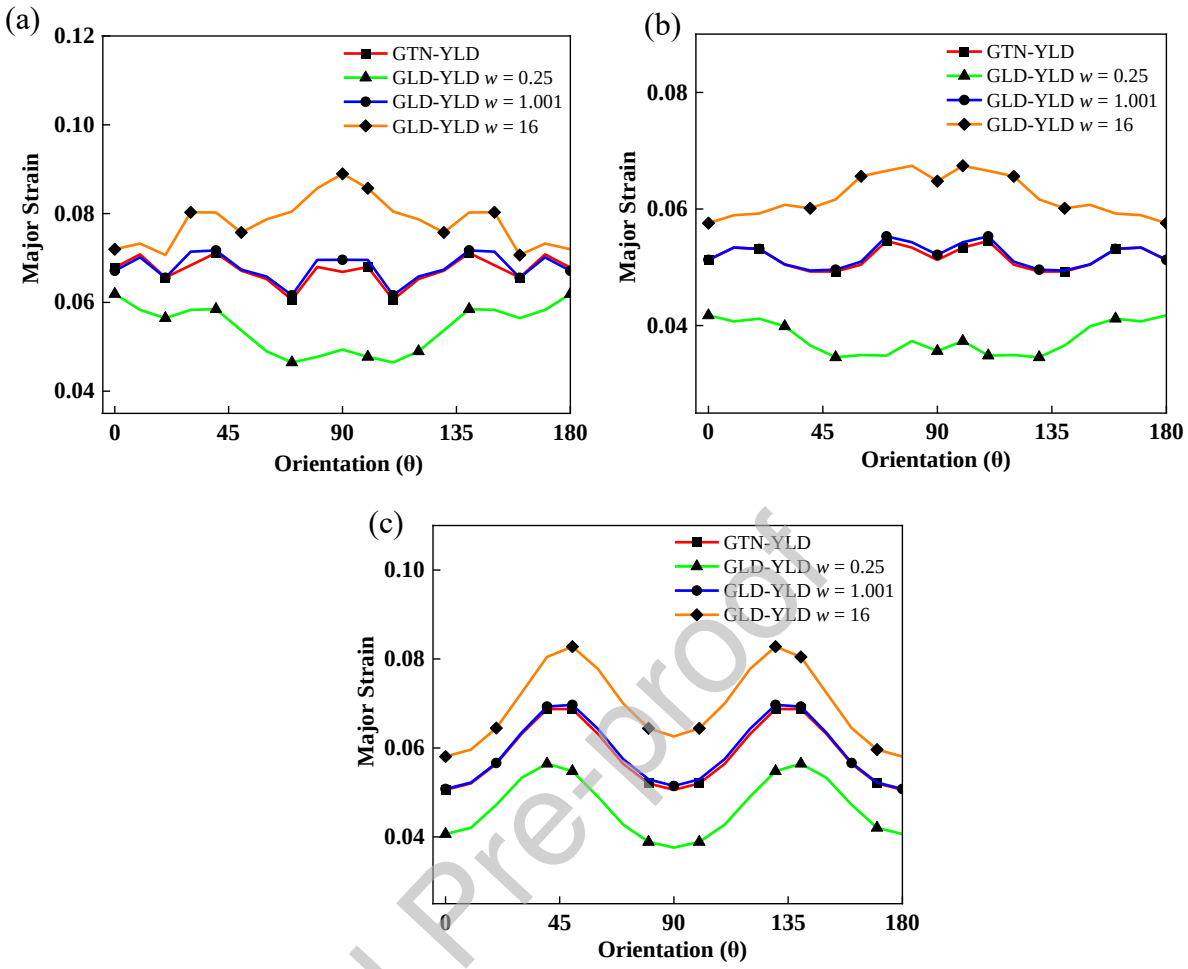

Fig. 17. Evolution of the major strain with respect to material orientation, for strong anisotropy material, for w=0.25, 1.001, and 16, and for: (a) uniaxial tension, (b) plane-strain tension, and (c) balanced biaxial tension.

In all the previous cases, the simplest form of the GLD-YLD coupled model was considered, where the rolling direction of the anisotropic matrix material was assumed to be perpendicular to the major axis of the ellipsoidal void, i.e., $\gamma = 90^{\circ}$ (see, Fig. 4). In this section, a more general case is considered to better simulate real-world conditions, where the rolling direction of the matrix material is not necessarily aligned with the void orientation. Fig. 18 illustrates the relative orientations of the ellipsoidal void, the matrix material rolling direction, and the major strain loading direction for both prolate and oblate voids. Two specific cases are investigated within this general GLD-YLD coupled constitutive model framework, corresponding to two different values of the angle between the void orientation and the rolling direction, i.e., $\gamma = 80^{\circ}$ and $\gamma = 45^{\circ}$. It is important to note that the rolling direction and the void orientation are fixed relative to the local x–y coordinate system, while the x–y system itself is rotated with respect to the global X_1–X_2 reference frame by an angle θ. The latter angle θ is

systematically varied from 0° to 180° in order to capture the complete coupled anisotropic material response.

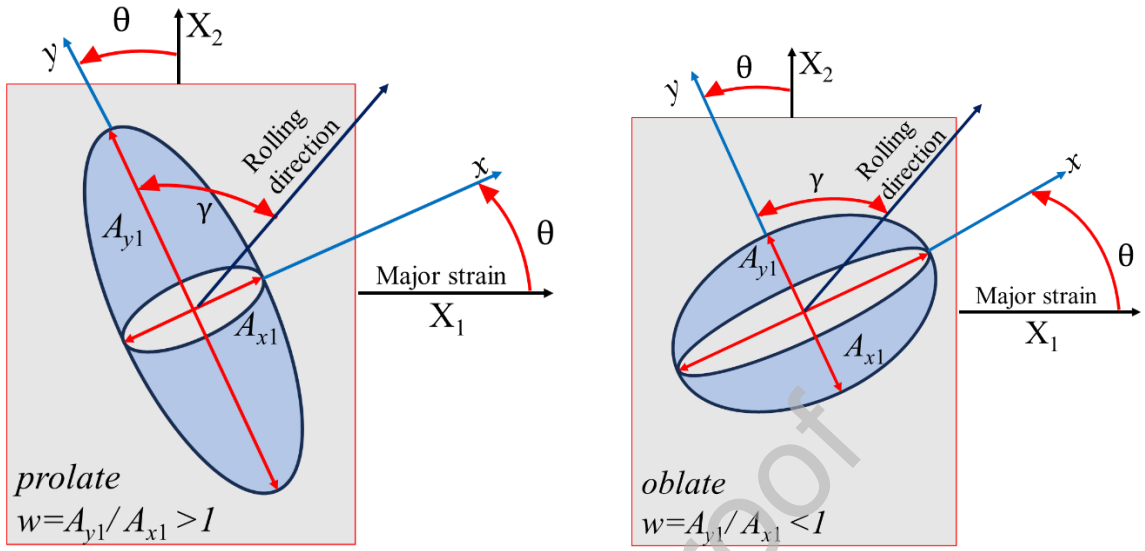

(a) (b)

Fig. 18. Illustration of void orientation, matrix material rolling direction, and major strain loading direction for: (a) prolate voids, and (b) oblate voids.

Figs. 19-20 illustrate the variation of major strains at localization with respect to material orientation θ, under three specific loading conditions: uniaxial tension (UT), plane-strain tension (PST), and balanced biaxial tension (BBT). An anisotropy misalignment of $\gamma = 80^{\circ}$ is considered in Fig. 19, while Fig. 20 corresponds to a misalignment of $\gamma = 45^{\circ}$. In the case of the GTN-YLD model, only the anisotropy of the matrix material is considered. Consequently, the anisotropy misalignment leads to a shift in the corresponding red curves in Fig. 19 and Fig. 20 by 10° and 45°, respectively, compared to the baseline curves in Fig. 17, while preserving their overall shape. Due to this shift, all the curves in Figs. 19-20 including the GLD-YLD model curves, are no longer symmetrical about the reference orientation of 90°, unlike those in Fig. 17. Furthermore, it is evident from these results that the major strain values are lowest for oblate voids (i.e., $w = 0.25$), followed by spherical voids ($w = 1$), and highest for prolate voids ($w = 16$). An exception is observed under balanced biaxial tension with anisotropy misalignment of $\gamma = 45^{\circ}$ at a specific range of material orientation, i.e., $20^{\circ} < \theta < 50^{\circ}$, where the major strains for oblate voids ($w = 0.25$) are unexpectedly high—exceeding those for prolate voids ($w = 16$), as shown in Fig. 20c. This peculiar behavior is likely due to a complex interplay of factors, including coupled matrix-induced and void-shape-induced anisotropy, the relative angle between the rolling direction and void orientation (γ), and void nucleation mechanisms. Despite this exception, the general trend remains consistent across all other loading conditions, material orientations (θ), and anisotropy

misalignment (γ): prolate voids exhibit higher major limit strains compared to oblate voids. These results highlight the complex anisotropic material behavior, driven by the combined effects of void shape-induced and matrix material anisotropy, as well as their relative alignment.

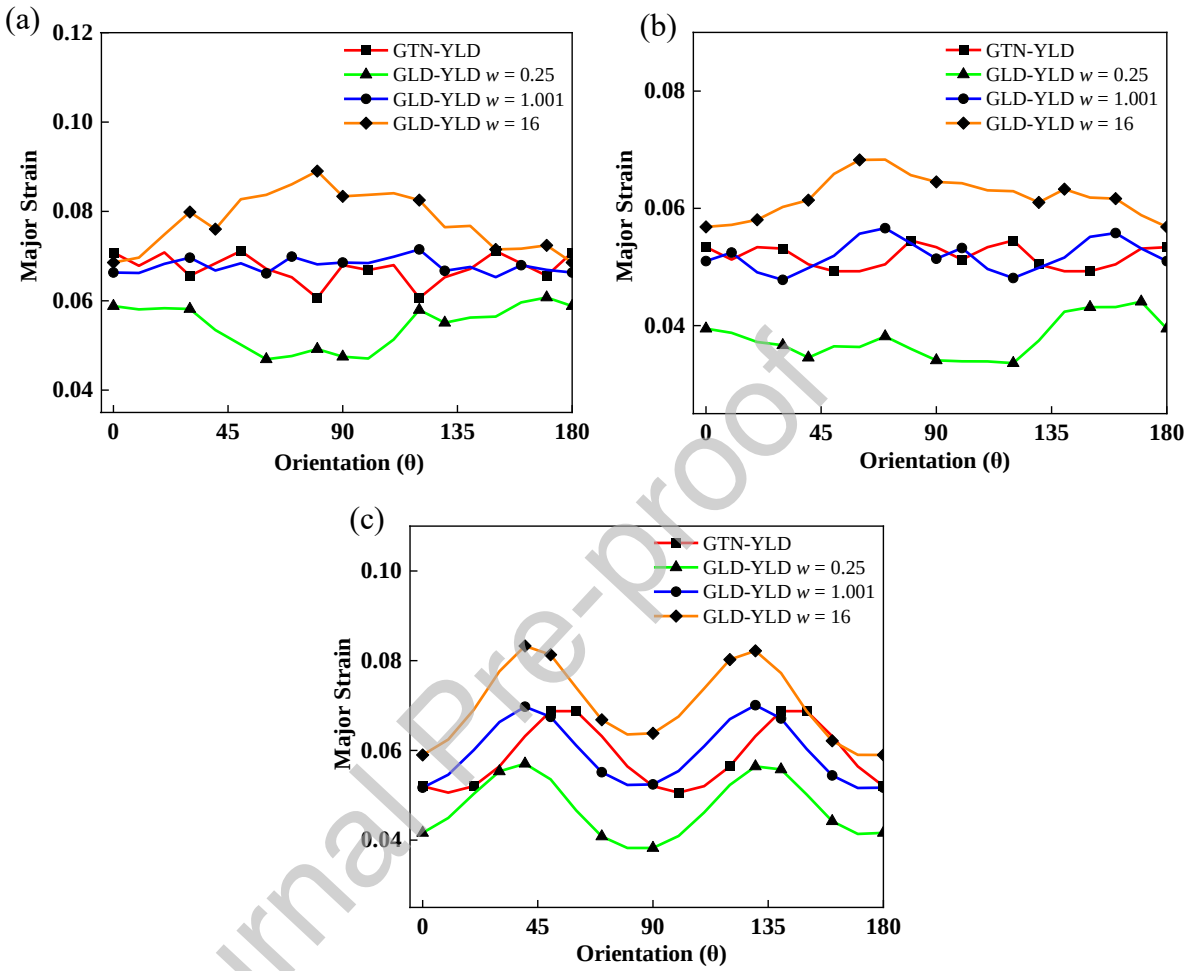

Fig. 19. Evolution of the major strain with respect to material orientation, for strong anisotropy material with $\gamma = 80^{\circ}$, for w=0.25, 1.001, and 16, and for: (a) uniaxial tension, (b) plane-strain tension, and (c) balanced biaxial tension.

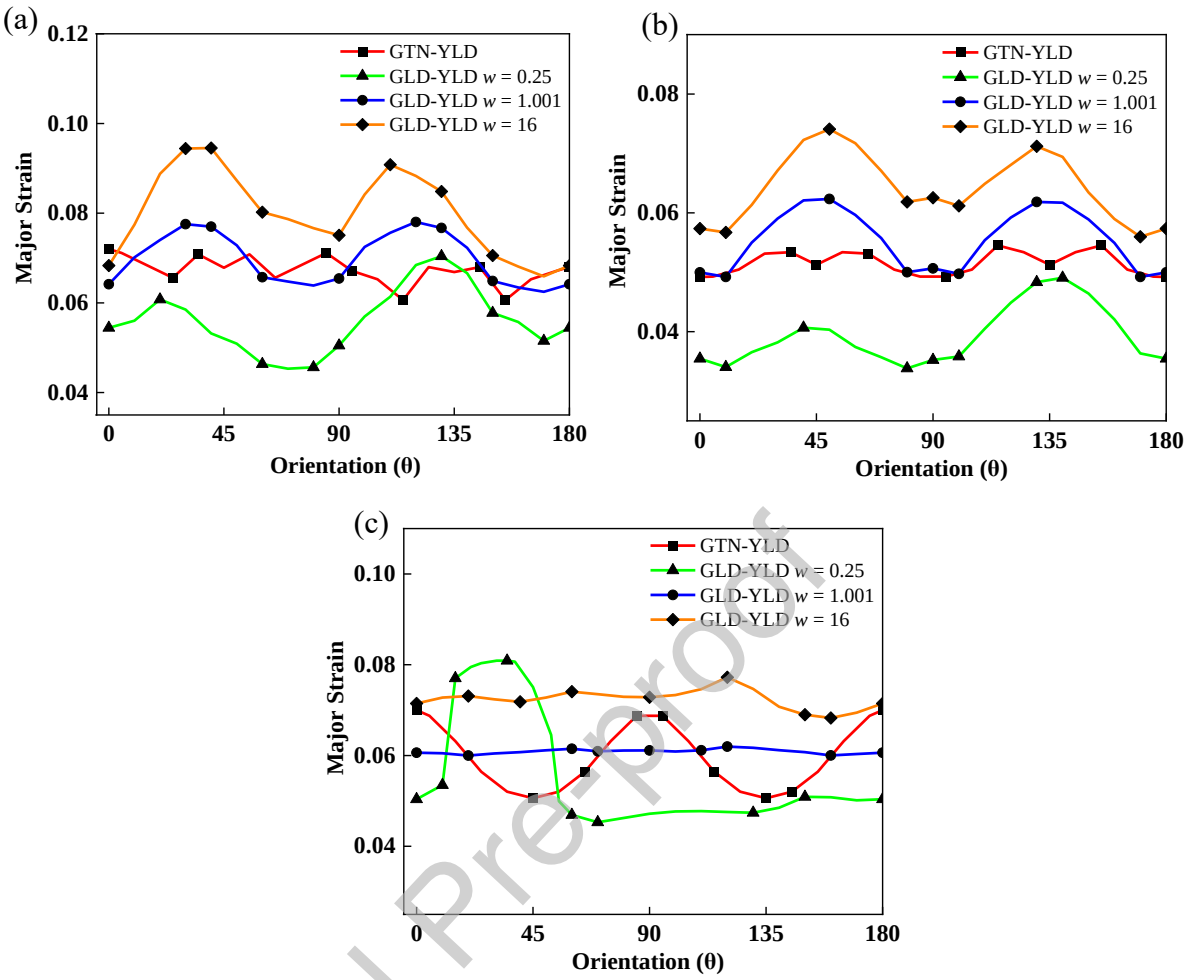

Fig. 20. Evolution of the major strain with respect to material orientation, for strong anisotropy material with $\gamma = 45^{\circ}$, for w=0.25, 1.001, and 16, and for: (a) uniaxial tension, (b) plane-strain tension, and (c) balanced biaxial tension.

5.2. FLD prediction for a real material 6111-T4

This subsection focuses on the prediction of FLDs for the aluminum alloy 6111-T4, a widely-used material in industrial applications. The relevant material parameters are listed in Table 2 and Table 3. Fig. 21 compares the predicted FLDs with the experimental data reported by Luo et al. [99]. Note that the initial geometric imperfection factor z_0, involved in the M–K localized necking criterion, is taken equal to 0.999, which allows predicting realistic limit strains with respect to the experimental data.

What characterizes the aluminum alloy 6111-T4 is that it is relatively only weakly damaged, due to its very low porosity, as outlined in Table 3 and discussed in the previous study (see Subsection 5.1.1). Therefore, the void shape effect on the predicted FLDs is not very significant. Nevertheless, a moderate increase in the forming limit strains is observed in Fig. 21 as the void aspect ratio increases from 0.25 (indicating oblate voids) to 16 (representing prolate voids). This reveals a slight sensitivity of the material formability to the void morphology.

Furthermore, Fig. 21 includes the FLD results obtained with the conventional von Mises model, which does not account for damage and anisotropy effects (i.e., J_2 elastic–plastic flow theory). It can be concluded from this comparison that, although the limit strains are close to the experimental data in the left-hand side of FLD, this classical undamaged isotropic model predicts unrealistically high forming limit strains in the right-hand side of the FLD, thus demonstrating its limitations for anisotropic materials like aluminum alloy 6111-T4. By contrast, the GLD-YLD coupled model, which integrates damage-induced anisotropy as well as dense matrix material anisotropy, provides a much closer agreement with the experimental results in the right-hand side of the FLD, underscoring its reliability and relevance for accurate prediction of FLDs. These results highlight the critical importance of incorporating damage and anisotropy effects in constitutive models to achieve realistic predictions of forming limit strains for aluminum alloys, especially for loading paths with positive strain path ratios. As to the loading paths with negative strain path ratios, the consideration of damage and anisotropy effects slightly lowers the predicted necking strains, compared to experimental values, resulting in an underestimation of formability limits. However, this conservative prediction, which poses no issue for design, provides an additional factor of safety in sheet metal forming processes.

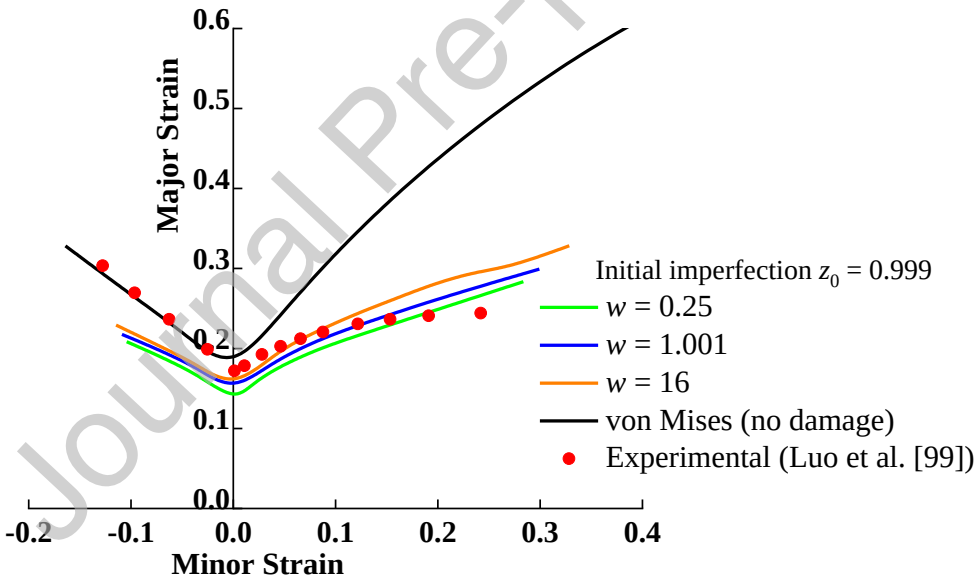

Fig. 21. Prediction of FLDs for aluminum alloy 6111-T4, using the GLD-YLD coupled model, with void aspect ratios of 0.25, 1.001, and 16, as well as the conventional von Mises model without damage and anisotropy.

5.3. FLD prediction for a real material 2090-T3

This subsection is devoted to the FLD predictions for 2090-T3 aluminum alloy by using the developed numerical tool based on the GLD-YLD coupled damage model. The predicted results are also compared with experimental data reported in the literature [100]. It is worth mentioning that for the 2090-T3 aluminum alloy, the material parameters available in the literature correspond to an

undamaged constitutive framework. Accordingly, the elastic, hardening, and anisotropy parameters were calibrated in the existing literature to accurately represent the material response under this assumption. The elasticity and isotropic hardening parameters, based on Swift's law, are reported in Grilo et al. [98]. Young's modulus and Poisson's ratio are taken as 70 GPa and 0.3, respectively. The Swift hardening parameters used are: $K = 646\text{MPa}, \varepsilon_0 = 0.025, \text{and } n = 0.227$. Additionally, the 19 anisotropy coefficients required for the YLD-2004-18p yield function are adopted from Barlat et al. [42] and are listed in Table 2.

To evaluate the model predictive capabilities, FLDs are predicted by using both the isotropic von Mises and the anisotropic YLD-2004-18p yield functions for the matrix material coupled with undamaged material model. It should be noted that, for this purpose, the initial porosity value in the GLD model is set to 0, while the void nucleation and void coalescence mechanisms are deactivated. Moreover, the initial void aspect ratio is considered as $w=1$, and its evolution during plastic deformation is also deactivated. The corresponding FLDs are presented in Fig. 22. The isotropic von Mises yield function overpredicts the forming limit strains under positive biaxial loading conditions. By contrast, incorporating non-quadratic anisotropy significantly improves the accuracy of the predictions, reducing the forming limit strains on the right-hand side of FLD to more realistic values. A good agreement is observed between the numerically predicted FLDs and the experimental data, thereby validating the model effectiveness.

Furthermore, to investigate the influence of void shape in porous ductile material on the FLD, the GLD model including damage is used this time, with weak damage parameters as those listed in Table 3. Three initial void aspect ratios are considered: 1.001, 0.25 (oblate), and 16 (prolate). The corresponding FLDs are represented in Fig. 22. As expected, the FLD exhibits a downward shift when damage is included in the material constitutive modeling (i.e., GLD model); however, this reduction in forming limit strains is small due to the weak nature of the damage parameters. It is interesting to note that even for an initially spherical void (i.e., $w\approx1$), the plastic deformation leads to void shape evolution, subsequently resulting in non-spherical prolate or oblate voids, and the GLD model effectively accounts for this phenomenon. Therefore, the incorporation of damage via the GLD constitutive model not only leads to a downward shift in the forming limit strains; but also alters the overall shape of the FLD compared to that yielded by the undamaged material model. Additionally, it can be observed from Fig. 22 that increasing the initial void aspect ratio from 0.25 to 16 leads to a slight upward shift in the FLD, although the effect remains small due to the weak damage parameters. These results provide further validation for the developed constitutive model, thus confirming its robust and efficient implementation within a MATLAB program.

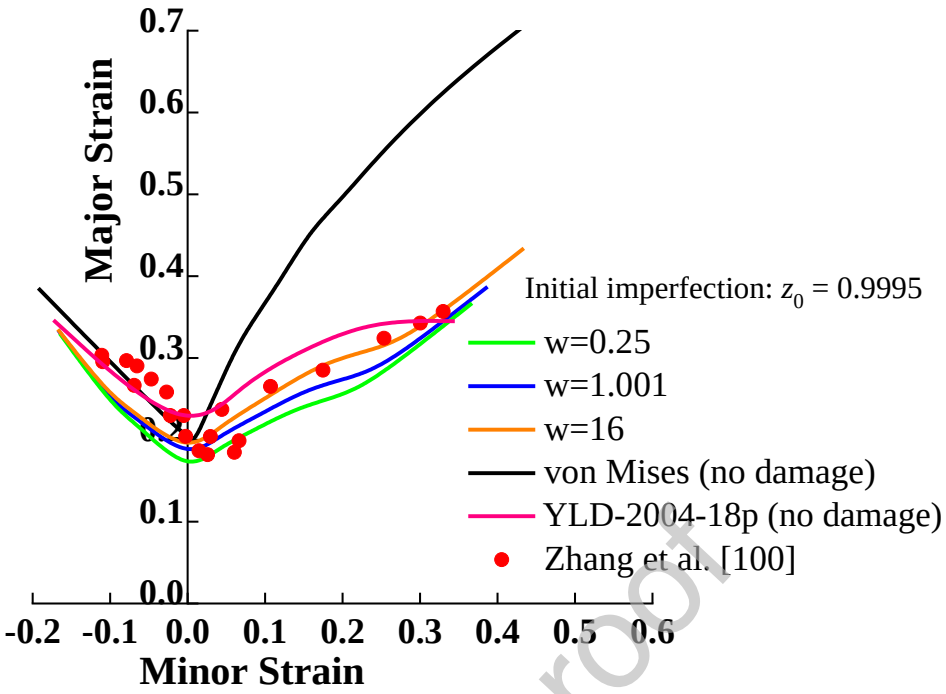

Fig. 22. Prediction of FLDs for aluminum alloy 2090-T3, using the GLD-YLD coupled model, with void aspect ratios of 0.25, 1.001, and 16, as well as the conventional isotropic von Mises model and anisotropic YLD-2004-18p model without damage.

5.4. FLD prediction for a fictitious material with strong anisotropy, strong damage and strong hardening parameters

It can be observed from the above results that the influence of void shape becomes more pronounced when the damage parameters (such as initial porosity, void nucleation, and void coalescence) correspond to a material with strong damage. The incorporation of such parameters leads to a significant reduction in the formability limit. To mitigate this reduction and analyze the influence of isotropic hardening parameters on the FLDs, high isotropic hardening parameters are now introduced. To this end, the FLD of a strongly anisotropic material (FM-08), characterized by severe damage parameters (as listed in Table 1), is evaluated. However, high Swift's hardening parameters are now considered, i.e., $K = 2000\text{MPa}$, $\varepsilon_0 = 0.05$, and $n = 0.8$. Three void orientations are considered, i.e., 0°, 45°, and 90°. This setup allows for a comprehensive study of the combined effects of hardening behavior, anisotropy, damage, void shape, and void orientation on the material formability. The FLDs for this fictitious material are presented in Fig. 23, for void aspect ratios of 0.25, 1.001, and 16, and material/void orientation of 0°, 45°, and 90°. For comparison, the FLDs corresponding to low hardening parameters are also re-plotted in Fig. 23. It can be observed from this comparison that enhanced work hardening, achieved by increasing the isotropic hardening parameters, leads to an overall increase in the formability limit. This trend holds true across all loading conditions and void orientations. However,

the extent of increase in formability limit is not uniform for all loading conditions and void aspect ratios. Specifically, for oblate voids with an aspect ratio w=0.25, and under balanced biaxial tension, the increase in formability limit due to enhanced hardening is least. This observation remains consistent across all void orientations. The influence of isotropic hardening on formability is most pronounced under uniaxial tension, followed by plane-strain tension, and is least significant under balanced biaxial tension. Summarizing, hardening has the greatest impact on the formability limit under negative strain path ratios (i.e., the left-hand side of the FLD), regardless of the void aspect ratio and material orientation. On the right-hand side of the FLD with positive strain path ratios, the effect of hardening is reduced, particularly for oblate voids compared to prolate voids. On the right-hand side of the FLD, the influence of damage-induced softening becomes more significant in determining the formability limit.

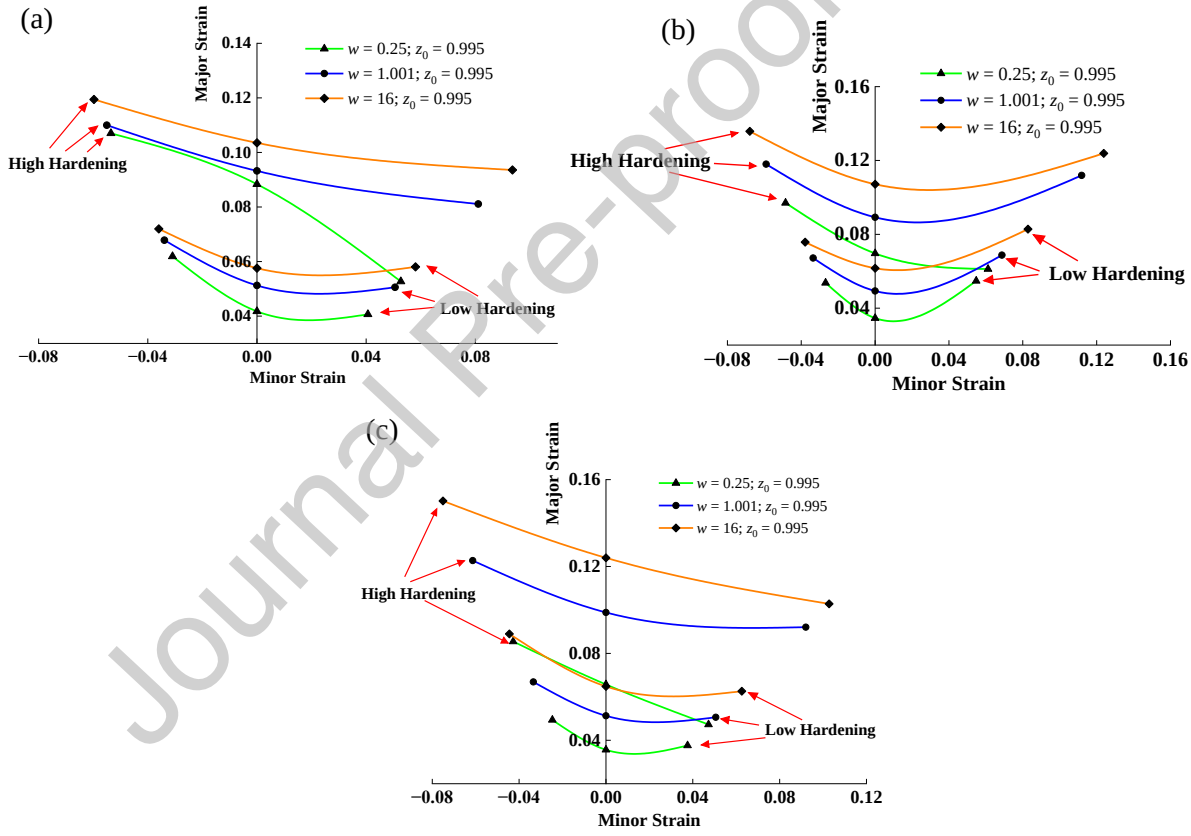

Fig. 23. FLDs for fictitious material with strong anisotropy, strong damage, and strong hardening parameters, for void aspect ratios of 0.25, 1.001, and 16, at: (a) 0° material orientation, (b) 45° material orientation, and (c) 90° material orientation.

6. Limitations and future work

This section outlines the key assumptions and limitations of the present simulations. It also highlights the potential directions for future research based on these considerations. In the present

contribution, void geometries limited to prolate and oblate shapes are considered within the framework of the GLD damage model. These geometries assume two equal axes and a third axis of different length (see, Fig. 24 in Appendix A), offering a simplified representation of porous ductile materials to initiate the study of void shape effects on material formability. However, this assumption does not fully capture the realistic void morphologies observed in porous ductile materials, which are more accurately described by arbitrary 3D ellipsoidal voids with all three unequal principal axes.

To address this, future research should consider the generalized Gurson-based damage model proposed by Madou and Leblond [35-36], which extends the constitutive framework to account for arbitrary 3D ellipsoidal voids. These models have been validated through finite element simulations for various void geometries [37]. The model has been further extended to develop void evolution laws [38], and combined isotropic and kinematic hardening [39]. These modifications are particularly relevant for accurately simulating loading conditions with low value of stress triaxiality ratio, as encountered in FLD predictions, where the stress triaxiality ratio typically ranges between 1/3 and 2/3. Therefore, future work should focus on implementing these generalized 3D void shape models, combined with advanced hardening laws, to enhance the prediction accuracy of FLDs. Additionally, these constitutive models can be extended to incorporate matrix material anisotropy, as in the present contribution, where YLD-2004-18p yield function defines the matrix material anisotropy.

The GLD-YLD coupled model developed in this contribution has been implemented in MATLAB. This approach is identical to a single-element approach with one integration point in the finite element analysis. For more comprehensive applications, future studies should embed this GLD-YLD coupled model and its extensions into a full finite element environment via user-defined material subroutines (UMAT or VUMAT) within commercial solvers, such as ABAQUS software. However, it is well recognized that damage-based constitutive models, exhibiting softening behavior, often suffer from mesh dependency in finite element simulations. To overcome this challenge, future work will also investigate regularization techniques, as proposed by Aravas and Xenos [22] in recent contribution, which mitigates mesh sensitivity through non-local formulations with appropriate material length scales.

Another promising extension is to couple the above-mentioned constitutive models with void-size-dependent Gurson-based models (see, e.g., [10-11]), allowing simultaneous consideration of isotropic hardening, kinematic hardening, non-quadratic anisotropy, void shape, and void-size effects. Such a comprehensive constitutive model would allow for a more realistic modeling of material behavior and accurate prediction of ductile failure.

Finally, implementing these advanced constitutive models in process simulations, such as deep drawing, represents an interesting direction for future research work. These simulations would be particularly valuable for optimizing manufacturing processes by enabling more accurate predictions of

material behavior. In particular, the anisotropic 3D constitutive models developed in this context are well-suited for modeling and predicting earing profiles, a common and critical defect in deep drawing processes. Furthermore, the inclusion of damage-induced softening effects enables the prediction of crack initiation and failure in complex 3D finite element simulations.

These limitations and directions for future research not only highlight the scope for advancing the present work, but also provide a roadmap for enhancing constitutive modeling in the context of ductile damage mechanics and metal forming processes.

7. Conclusions

This work provides a comprehensive analysis of the effects of void shape and void orientation on the prediction of forming limit diagrams (FLDs) for porous anisotropic materials, along with the investigation of anisotropy effects induced by changes in void aspect ratio and void orientation. The void shape and its orientation have been accounted for by following the GLD constitutive modeling framework, which considers voided materials with initially ellipsoidal cavities. Moreover, the GLD model has been extended to account for the plastic anisotropy of the dense matrix material, following Barlat's YLD-2004-18p non-quadratic anisotropic yield surface. The resulting anisotropic GLD-YLD coupled model has been combined with the M–K imperfection approach for the prediction of FLDs for various anisotropic sheet metals.

In the first part of the investigation, it was shown that, regardless of the degree of plastic anisotropy, prolate (needle-like) voids exhibit higher formability than oblate (plate-like) voids, while spherical voids yield intermediate behavior. The material orientation also has a strong impact on the predicted limit strains for all loading paths, due to the combined effects of void shape-induced and metal matrix-induced anisotropy. These findings highlight the pronounced impact of anisotropy on material formability, as a result of the mutual influence of two anisotropic factors: the void shape and its orientation, and the matrix material texture. The coupled material anisotropy is symmetrical about 90^o (i.e., the transverse direction) and repeats the same behavior after 180^o, due to the symmetrical void shape about transverse direction and the YLD-2004-18p yield function.

Additionally, the effect of misalignment between the rolling direction of the anisotropic matrix material and the major axis of ellipsoidal voids on material formability is investigated. Two misalignment cases were considered, i.e., 45^o and 80^o. It has been revealed that, for this misaligned anisotropic material, the initially observed 90^o symmetry does not hold any longer. Moreover, for the 45° misalignment, peculiar behavior was observed in the orientation range of 20°–50°, where the major strains for oblate voids unexpectedly exceeded those for prolate voids. This behavior is likely due to a

complex interplay of factors, including coupled matrix-induced and void-shape-induced anisotropy, the relative angle between the rolling direction and void orientation, and void nucleation mechanisms.

The second part of the study focused on predicting the FLD for two real aluminum alloys. To assess predictive capabilities, the GLD-YLD model results were compared with both the undamaged isotropic von Mises model and experimental FLDs from the literature. Overall, the simulation results displayed slight sensitivity of the material formability to void morphology, due to very low porosity of the studied aluminum alloys. Furthermore, although the GLD-YLD coupled model slightly underestimates the limit strains in the left-hand side of FLD, its predictions are in much closer agreement with the experimental results in the right-hand side of the FLD, where the undamaged isotropic model predicts unrealistically high forming limits.

In addition, the effect of isotropic hardening was also examined. It was demonstrated that enhanced work hardening increases the overall formability limit. However, the extent of increase is least for oblate voids under balanced biaxial tension. It can be concluded that isotropic hardening has the greatest impact on the formability limit under negative strain path ratios (i.e., the left-hand side of the FLD), regardless of the void aspect ratio and material orientation. By contrast, at positive strain paths (right-hand side of the FLD), the effects are reduced, particularly for oblate voids, where damage-induced softening dominates in determining the formability limit.

These results underscore the critical importance of simultaneously incorporating dense matrix material anisotropy, damage-induced anisotropy and isotropic hardening into constitutive modeling for accurate FLD prediction.

Appendix A. Representative volume element and confocal ellipsoidal voids considered in the GLD damage model

The representative volume elements, with the incorporated voids, that are considered in the GLD damage model are presented in Fig. 24.

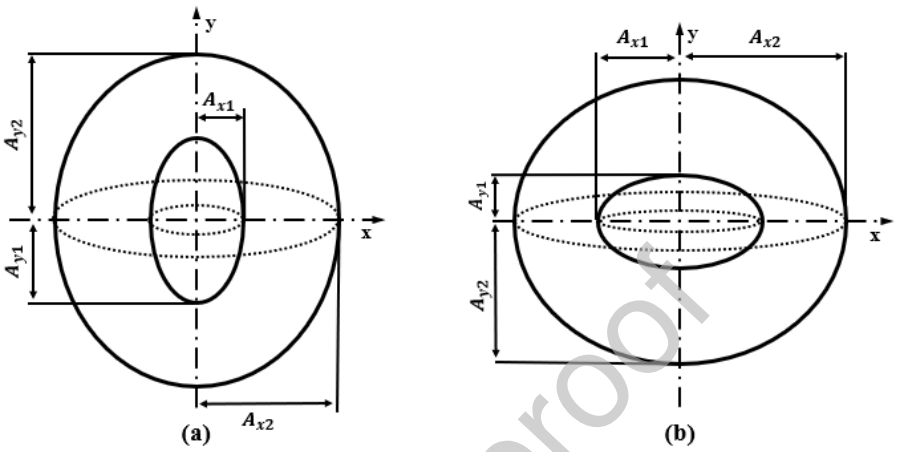

Fig. 24. The representative volume element and the incorporated ellipsoidal void in the GLD damage model: (a) prolate, and (b) oblate.

The focal distance c, void aspect ratio w, and eccentricities of the void and RVE are given by the following relations:

$$w = aspect\ ratio = \frac{A_{y2}}{A_{x2}} = \frac{A_{y1}}{A_{x1}}, \tag{A.1}$$

$$c = focal\ distance = \sqrt{\left|A_{x_2}^2 - A_{y_2}^2\right|} = \sqrt{\left|A_{x_1}^2 - A_{y_1}^2\right|}, \tag{A.2}$$

$$e_1 = eccentricity\ of\ void = \begin{cases} \dfrac{c}{A_{y_1}} & (P) \\ \dfrac{c}{A_{x_1}} & (O) \end{cases}, \tag{A.3}$$

and

$$e_2 = eccentricity\ of\ RVE = \begin{cases} \dfrac{c}{A_{y_2}} & (P) \\ \dfrac{c}{A_{x_2}} & (O) \end{cases}. \tag{A.4}$$

Given a porosity f and an aspect ratio $S = ln(w)$, we can calculate the eccentricities e_1 and e_2 defined in Eqs. (A.3) and (A.4) by solving the following relations:

$$e_1^2 = 1 - \exp(-2|S|), \tag{A.5}$$

and

$$\begin{cases} \dfrac{f\left(1-e_2^2\right)}{e_2^3} = \dfrac{1-e_1^2}{e_1^3} & (P) \\ \dfrac{f\sqrt{\left(1-e_2^2\right)}}{e_2^3} = \dfrac{\sqrt{1-e_1^2}}{e_1^3} & (O) \end{cases}, \tag{A.6}$$

where (P) and (O) stand for a shorthand notation for prolate and oblate voids, respectively.

Appendix B. Important expressions required for the GLD damage model

The parameter α_2, used for the calculation of the modified hydrostatic stress Σ_h in the GLD model, is given as (see [101]):

$$\alpha_2 = \begin{cases} \dfrac{1+e_2^2}{3+e_2^4} & (P) \\ \dfrac{\left(1-e_2^2\right)\left(1-2e_2^2\right)}{3-6e_2^2+4e_2^4} & (O) \end{cases}. \tag{B.1}$$

In addition, C, η, g, κ and q are functions of f and S. Their relationships are given as follows (see [28,101]):

$$C = -\frac{\kappa(g+1)(g+f)sh}{\eta(Q+\eta H)}, \tag{B.2}$$

$$\eta = -\frac{\kappa Q(g+1)(g+f)sh}{(g+1)^2+(g+f)^2+(g+f)(g+1)[\kappa Hsh-2ch]}, \tag{B.3}$$

$$g = \begin{cases} 0 & (P) \\ \dfrac{e_2^3}{\sqrt{1-e_2^2}} & (O) \end{cases}, \tag{B.4}$$

$$\kappa^{-1}=\begin{cases}\dfrac{1}{\sqrt{3}}+\dfrac{1}{\ln(f)}\left\{\left(\sqrt{3}-2\right)\ln\left(\dfrac{e_1}{e_2}\right)-\dfrac{1}{\sqrt{3}}\ln\left(\dfrac{3+e_1^2+2\sqrt{3+e_1^4}}{3+e_2^2+2\sqrt{3+e_2^4}}\right)+\ln\left(\dfrac{\sqrt{3}+\sqrt{3+e_1^4}}{\sqrt{3}+\sqrt{3+e_2^4}}\right)\right\} & (P)\\ \dfrac{2}{3}+\dfrac{\dfrac{2}{3}\left(g_f-g_1\right)+\dfrac{2}{5}\left(g_f^{5/2}-g_1^{5/2}\right)\left(\dfrac{4}{3}-g_f^{5/2}-g_1^{5/2}\right)}{\ln\left(\dfrac{g_f}{g_1}\right)};g_f=\dfrac{g}{g+f};g_1=\dfrac{g}{g+1} & (O)\end{cases}, \quad \text{(B.5)}$$

$$q=1+2\left(q_0-1\right)\frac{e^S}{1+e^{2S}}\ , \quad \text{(B.6)}$$

where

$$Q=1-f\ , \quad \text{(B.7)}$$

$$H=2\left(\alpha_1-\alpha_2\right), \quad \text{(B.8)}$$

$$ch=\cosh(\kappa H), \quad \text{(B.9)}$$

and

$$sh=\sinh(\kappa H)\ . \quad \text{(B.10)}$$

Here, q_0 is the value of q typically selected in the original Gurson damage model for spherical voids.

Appendix C. Evolution equations of the internal variables in the GLD model

The evolution equations of the three internal variables f, S and $\bar{\sigma}$ are given as follows (see [33]):

$$\dot{f}=\dot{f}_G+\dot{f}_N, \quad \text{(C.1)}$$

$$\dot{S}=\frac{3}{2}\xi_1\left(\mathbf{D}^p:\mathbf{X}\right)+\xi_2 tr\left(\mathbf{D}^p\right), \quad \text{(C.2)}$$

and

$$\dot{\bar{\sigma}}=\frac{\partial\bar{\sigma}}{\partial\bar{\varepsilon}^p}\dot{\bar{\varepsilon}}^p=h\dot{\bar{\varepsilon}}^p\ . \quad \text{(C.3)}$$

Here, the evolution of the porosity $\dot{f}$ is partitioned as the contribution of void growth $\dot{f}_G$ and that of void nucleation $\dot{f}_N$. As per Gao et al. [33]:

$$\dot{f}_G=\left(1-f\right)tr\left(\mathbf{D}^p\right). \quad \text{(C.4)}$$

Additionally, strain-controlled void nucleation, as modeled by Chu and Needleman [6] using a normal distribution function, is considered:

$$\dot{f}_N = \frac{\psi}{s_N\sqrt{2\pi}}\exp\left(-\frac{1}{2}\left(\frac{\bar{\varepsilon}^p - \varepsilon_N}{s_N}\right)^2\right)\dot{\bar{\varepsilon}}^p = A_N\dot{\bar{\varepsilon}}^p, \tag{C.5}$$

where ψ represents the void volume fraction of cavities that are likely to nucleate, ε_N and s_N are the mean strain and standard deviation of the normal distribution, respectively. In the present constitutive model, void coalescence has also been incorporated in addition to void growth and void nucleation. Tvergaard and Needleman [102] modeled the void coalescence regime by introducing the concept of effective porosity denoted by $f^*(f)$. According to their phenomenological coalescence model, void coalescence occurs when the value of porosity reaches the critical porosity f_{cr}, which then accelerates the decay of material load carrying capacity. The relationship for effective porosity is given as:

$$f^* = f_{cr} + \delta_{GTN}(f - f_{cr}). \tag{C.6}$$

In the above relation, δ_{GTN} is the accelerating factor, while both the f_{cr} and δ_{GTN} are considered as material parameters. The accelerating factor δ_{GTN} is equal to 1 before the onset of coalescence (i.e., when $f \le f_{cr}$), and becomes greater than 1 once the coalescence regime activates (i.e., $f > f_{cr}$).

In Eq. (C.2), ξ_1 and ξ_2 are defined as follows (see [27, 28]):

$$\xi_1 = 1 + \frac{9}{2}\xi_T\left(1-\sqrt{f}\right)^2\frac{\alpha_1 - \alpha_1'}{1-3\alpha_1}, \tag{C.7}$$

$$\xi_2 = \frac{1-3\alpha_1}{f} + 3\alpha_2 - 1, \tag{C.8}$$

where

$$\xi_T = 1 - \frac{T^2 + T^4}{9}. \tag{C.9}$$

In above equations, α_1, the stress triaxiality ratio *T*, and α_1' are defined as follows (see [24, 28]):

$$\alpha_1 = \begin{cases} \dfrac{1}{2e_1^2} - \dfrac{1-e_1^2}{2e_1^3}\tanh^{-1}(e_1) & (P) \\ -\dfrac{1-e_1^2}{2e_1^2} + \dfrac{\sqrt{1-e_1^2}}{2e_1^3}\sin^{-1}(e_1) & (O) \end{cases}, \tag{C.10}$$

$$T = \frac{\Sigma_m}{\Sigma_{eq}}, \tag{C.11}$$

where $\Sigma_m = \frac{1}{3}(\boldsymbol{\Sigma}:\mathbf{I})$ is the mean stress, and Σ_{eq} is the equivalent stress, which accounts for plastic anisotropy of the dense matrix material, and

$$\alpha_1' = \begin{cases} \dfrac{1}{3-e_1^2} & (P) \\ \dfrac{1-e_1^2}{3-2e_1^2} & (O) \end{cases}. \tag{C.12}$$

Declaration of conflicting interests

The Authors declare that there is no conflict of interest.

References

[1] Keeler SP. Plastic instability and fracture in sheets stretched over rigid punches. Massachusetts Institute of Technology 1961.

[2] Goodwin GM. Application of strain analysis to sheet metal forming problems in the press shop. Sae Transactions 1968;77:380-387.

[3] Nakazima K, Kikuma T, Hasuka K. Study on the formability of steel sheets. Yamata Tech Report 1968;264:8517-8530.

[4] Erichsen A. A new test for thin sheets. Stahl und Eisen 1914;34:879-882.

[5] Gurson AL. Continuum theory of ductile rupture by void nucleation and growth: Part I—Yield criteria and flow rules for porous ductile media. Journal of Engineering Materials and Technology 1977;99:2-15.

[6] Chu C, Needleman A. Void nucleation effects in biaxially stretched sheets. Journal of Engineering Materials and Technology 1980;102:249-256.

[7] Tvergaard V. Material failure by void coalescence in localized shear bands. International Journal of Solids and Structures 1982;18:659-672.

[8] Lacroix R, Leblond J-B, Perrin G. Numerical study and theoretical modelling of void growth in porous ductile materials subjected to cyclic loadings. European Journal of Mechanics-A/Solids 2016;55:100-109.

[9] Morin L, Michel J-C, Leblond J-B. A Gurson-type layer model for ductile porous solids with isotropic and kinematic hardening. International Journal of Solids and Structures 2017;118:167-178.

[10] Wen J, Huang Y, Hwang K, Liu C, Li M. The modified Gurson model accounting for the void size effect. International Journal of Plasticity 2005;21:381-395.

[11] Dormieux L, Kondo D. An extension of Gurson model incorporating interface stresses effects. International Journal of Engineering Science 2010;48:575-581.

[12] Wu H, Zhuang X, Zhang W, Zhao Z. Anisotropic Gurson–Tvergaard–Needleman model considering the anisotropic void behaviors. International Journal of Mechanical Sciences 2023;248:108229.

[13] Wu H, Zhuang X, Zhang W, Zhao Z. Anisotropic ductile fracture: Experiments, modeling, and numerical simulations. Journal of Materials Research and Technology 2022;20:833-856.

[14] Rahman MA, Uddin MM, Kabir L. Experimental Investigation of Void Coalescence in XTral-728 Plate Containing Three-Void Cluster. European Journal of Engineering and Technology Research 2024;9(1):60-65.

[15] Khan IA, Benallal A, Benzerga AA, Moussy F, Needleman A. Localized necking predictions for an imperfect sheet using a porous plastic constitutive relation with two porosity parameters. Engineering Fracture Mechanics 2025;314:110711.

[16] Zhou J, Gao X, Sobotka JC, Webler BA, Cockeram BV. On the extension of the Gurson-type porous plasticity models for prediction of ductile fracture under shear-dominated conditions. International Journal of Solids and Structures 2014;51:3273-3291.

[17] Nahshon K, Hutchinson J. Modification of the Gurson model for shear failure. European Journal of Mechanics-A/Solids 2008;27:1-17.

[18] Khan IA, Benzerga AA, Needleman A. A shear modified enhanced Gurson constitutive relation and implications for localization. Journal of the Mechanics and Physics of Solids 2023;171:105153.

[19] Pardoen T, Kaniadakis A, Nguyen VD, Noels L, Javangorough S, Besson J. Modelling and 3D simulation of ductile crack growth with non-local Gurson-based formulation. European Journal of Mechanics-A/Solids 2025:105772.

[20] Zhang T, Zhao Y. A study on the parameter identification and failure prediction of ductile metals using Gurson–Tvergaard–Needleman (GTN) model. Materials Today Communications 2023;34:105223.

[21] Bensaada R, Imad A, Kanit T, Moumen AE, Almansba M, Saouab A. Phenomenological–based strategy for the Gurson-Tvergaard-Needleman model parameters identification. Applications in Engineering Science 2025:100243.

[22] Aravas N, Xenos S. "Implicit" vs "Explicit" gradient plasticity models: Do they always remove mesh dependence in softening materials? International Journal of Solids and Structures 2023;281:112415.

[23] Wang Y, Zhu Y, Zhao L, Liang S, Huang M, Li Z. A statistical yield model for porous polycrystals. European Journal of Mechanics-A/Solids 2025;111:105534.

[24] Gologanu M, Leblond J-B, Devaux J. Approximate models for ductile metals containing non-spherical voids—case of axisymmetric prolate ellipsoidal cavities. Journal of the Mechanics and Physics of Solids 1993;41:1723-1754.

[25] Gologanu M, Leblond J-B, Devaux J. Approximate models for ductile metals containing nonspherical voids—case of axisymmetric oblate ellipsoidal cavities. Journal of Engineering Materials and Technology 1994;116:290-297.

[26] Gologanu M, Leblond J-B, Perrin G, Devaux J. Recent extensions of Gurson's model for porous ductile metals. Continuum micromechanics. Springer 1997:61-130.

[27] Pardoen T, Hutchinson J. An extended model for void growth and coalescence. Journal of the Mechanics and Physics of Solids 2000;48:2467-2512.

[28] Gologanu M, Leblond J-B, Perrin G, Devaux J. Theoretical models for void coalescence in porous ductile solids. I. Coalescence "in layers". International Journal of Solids and Structures 2001;38:5581-5594.

[29] Gologanu M, Leblond J-B, Devaux J. Theoretical models for void coalescence in porous ductile solids. II. Coalescence "in columns". International Journal of Solids and Structures 2001;38:5595-5604.

[30] Benzerga AA. Micromechanics of coalescence in ductile fracture. Journal of the Mechanics and Physics of Solids 2002;50:1331-1362.

[31] Benzerga AA, Besson J. Plastic potentials for anisotropic porous solids. European Journal of Mechanics-A/Solids 2001;20:397-434.

[32] Benzerga AA, Leblond J-B. Ductile fracture by void growth to coalescence. Advances in Applied Mechanics 2010;44:169-305.

[33] Gao X, Wang T, Kim J. On ductile fracture initiation toughness: Effects of void volume fraction, void shape and void distribution. International Journal of Solids and Structures 2005;42:5097-5117.

[34] Enakoutsa K, Li Y. Metal plasticity and nonlocal damage modeling: A thermodynamically consistent GSM approach with computational implications. Mathematics and Mechanics of Solids 2025:10812865251321427.

[35] Madou K, Leblond J-B. A Gurson-type criterion for porous ductile solids containing arbitrary ellipsoidal voids—I: Limit-analysis of some representative cell. Journal of the Mechanics and Physics of Solids 2012;60:1020-1036.

[36] Madou K, Leblond J-B. A Gurson-type criterion for porous ductile solids containing arbitrary ellipsoidal voids—II: Determination of yield criterion parameters. Journal of the Mechanics and Physics of Solids 2012;60:1037-1058.

[37] Madou K, Leblond J-B. Numerical studies of porous ductile materials containing arbitrary ellipsoidal voids–I: Yield surfaces of representative cells. European Journal of Mechanics-A/Solids 2013;42:480-489.

[38] Madou K, Leblond J-B, Morin L. Numerical studies of porous ductile materials containing arbitrary ellipsoidal voids–II: Evolution of the length and orientation of the void axes. European Journal of Mechanics-A/Solids 2013;42:490-507.

[39] Roubaud F, Morin L, Remmal A, Marie S, Leblond JB. A Gurson-type layer model for ductile porous solids containing ellipsoidal voids with isotropic and kinematic hardening. European Journal of Mechanics-A/Solids 2024;104:105114.

[40] Xenos S, Aravas N, Danas K. A homogenization-based model of the Gurson type for porous metals comprising randomly oriented spheroidal voids. European Journal of Mechanics-A/Solids 2024;105:105238.

[41] Hosseini N, Nieto-Fuentes JC, Dakshinamurthy M, Rodríguez-Martínez JA, Vadillo G. The effect of material orientation on void growth. International Journal of Plasticity 2022;148:103149.

[42] Barlat F, Aretz H, Yoon JW, Karabin M, Brem J, Dick R. Linear transfomation-based anisotropic yield functions. International Journal of Plasticity 2005;21:1009-1039.

[43] Kumar S, Samal MK, Singh PK, Chattopadhyay J. Evolution of shape and size of voids under shear dominated loading conditions in ductile materials. Engineering Fracture Mechanics 2020;236:107208.

[44] Usman M, Waheed S, Mubashar A. Effect of shape on void growth: A coupled Extended Finite Element Method (XFEM) and Discrete Dislocation Plasticity (DDP) study. European Journal of Mechanics - A/Solids 2022;92:104471.

[45] Li Z, Steinmann P. RVE-based studies on the coupled effects of void size and void shape on yield behavior and void growth at micron scales. International Journal of Plasticity 2006;22:1195-1216.

[46] Son HS, Kim YS. Prediction of forming limits for anisotropic sheets containing prolate ellipsoidal voids. International Journal of Mechanical Sciences 2003;45:1625-1643.

[47] Son H-S, Kim Y-S, Na K-H, Hwang S-M. Effect of void shape and its growth on forming limits for anisotropic sheets containing non-spherical voids. JSME International Journal Series A Solid Mechanics and Material Engineering 2004;47:512-520.

[48] Choi SG, Son HS, Kim YS. Prediction of forming limits for anisotropic sheets with ellipsoidal voids. Key Engineering Materials 2004;274:397-402.

[49] Kim J, Zhang G, Gao X. Modeling of ductile fracture: Application of the mechanism-based concepts. International Journal of Solids and Structures 2007;44:1844-1862.

[50] Enakoutsa K, Bills YL. Moving from theory to application: Evaluating the numerical implementation of void shape effects and damage delocalization in the modeling of ductile fracture in porous plastic metals. Mathematics and Mechanics of Solids 2024;29:1432-1456.

[51] Nielsen KL. Predicting failure response of spot welded joints using recent extensions to the Gurson model. Computational Materials Science 2010;48:71-82.

[52] Legarth BN, Tvergaard V. Effects of plastic anisotropy and void shape on full three-dimensional void growth. Journal of Applied Mechanics 2018;85:051007.

[53] Keralavarma SM, Hoelscher S, Benzerga AA. Void growth and coalescence in anisotropic plastic solids. International Journal of Solids and Structures 2011;48:1696-1710.

[54] Barlat F, Lian K. Plastic behavior and stretchability of sheet metals. Part I: A yield function for orthotropic sheets under plane stress conditions. International Journal of Plasticity 1989;5:51-66.

[55] Marciniak Z, Kuczyński K. Limit strains in the processes of stretch-forming sheet metal. International Journal of Mechanical Sciences 1967;9:609-620.

[56] Marciniak Z. Analysis of necking preceding fracture of sheet metal under tension. Mettalurgia Italiana 1968;60:701-709.

[57] Marciniak Z, Kuczyński K, Pokora T. Influence of the plastic properties of a material on the forming limit diagram for sheet metal in tension. International Journal of Mechanical Sciences 1973;15:789-800.

[58] Hutchinson J, Neale K. Sheet necking-II. Time-independent behavior. Mechanics of Sheet Metal Forming: Material Behavior and Deformation Analysis. Springer 1978:127-153.

[59] Yamamoto H. Conditions for shear localization in the ductile fracture of void-containing materials. International Journal of Fracture 1978;14:347-365.

[60] Banabic D. A review on recent developments of Marciniak-Kuczynski model. Computer Methods in Materials Science 2010;10:225-237.

[61] Banabic D, Kami A, Comsa D-S, Eyckens P. Developments of the Marciniak-Kuczynski model for sheet metal formability: A review. Journal of Materials Processing Technology 2021;287:116446.

[62] Stören S, Rice J. Localized necking in thin sheets. Journal of the Mechanics and Physics of Solids 1975;23:421-441.

[63] Choi W, Gillis PP, Jones S. Calculation of the forming limit diagram. Metallurgical Transactions A 1989;20:1975-1987.

[64] Pishbin H, Gillis PP. Forming limit diagrams calculated using Hill's nonquadratic yield criterion. Metallurgical Transactions A 1992;23:2817-2831.

[65] Zhao L, Sowerby R, Sklad M. A theoretical and experimental investigation of limit strains in sheet metal forming. International Journal of Mechanical Sciences 1996;38:1307-1317.

[66] Vacher P, Arrieux R, Tabourot L. Analysis of a criterion of deep drawing operation capability for thin orthotropic sheets. Journal of Materials Processing Technology 1998;78:190-197.

[67] Nasir MW, Chalal H, Abed-Meraim F. Comparison between the Marciniak and Kuczyński imperfection approach and bifurcation theory in the prediction of localized necking for porous ductile materials. The International Journal of Advanced Manufacturing Technology 2022;119(7):5047-5068.

[68] Mansouri LZ, Chalal H, Abed-Meraim F. Ductility limit prediction using a GTN damage model coupled with localization bifurcation analysis. Mechanics of Materials 2014;76:64-92.

[69] Chalal H, Abed-Meraim F. Hardening effects on strain localization predictions in porous ductile materials using the bifurcation approach. Mechanics of Materials 2015;91:152-166.

[70] Dasappa P, Inal K, Mishra R. The effects of anisotropic yield functions and their material parameters on prediction of forming limit diagrams. International Journal of Solids and Structures 2012;49:3528-3550.

[71] Dewangan YK, Gupta A, Bandyopadhyay K, Faye A, Lee MG. Incorporation of anisotropy for the failure prediction of AA6061 during SPIF process. The International Journal of Advanced Manufacturing Technology 2025;136(1):279-296.

[72] Bressan JD. Analytical modelling of forming limit curves and the Lankford coefficients of anisotropy, r-values, using the non-associated Barlat´s Yld 2000-2d plastic potential. International Journal of Material Forming 2025;18(3):1-2.

[73] Mu Z, Hou T, He L, Liu J, Ma S, Yan H, Dai X. Understanding Anisotropy and Forming Limit in 6C16 Aluminum Alloy: Insights from Evolutionary R-Values with Various Calculation Methods. Metals and Materials International 2025:1-20.

[74] Chen X, Wang Z, Zhang X, Dong G, Yang Z, Yu S, Wang Y, Yang Y. Parameter calibration of anisotropic GTN model and forming limit for S600 aluminum alloy sheet. Engineering Research Express 2025;7(2):025419.

[75] Engler O. Correlating crystallographic texture with anisotropic properties and sheet metal forming of aluminium alloys. Journal of Materials Research and Technology 2025;35:514-522.

[76] Djavanroodi F, Ebrahimi M, Janbakhsh M. A study on the stretching potential, anisotropy behavior and mechanical properties of AA7075 and Ti-6Al-4V alloys using forming limit diagram: An experimental, numerical and theoretical approaches. Results in Physics 2019;14:102496.

[77] Nasir MW, Chalal H, Abed-Meraim F. Formability prediction using bifurcation criteria and GTN damage model. International Journal of Mechanical Sciences 2021;191:106083.

[78] Morin D, Hopperstad OS, Benallal A. On the description of ductile fracture in metals by the strain localization theory. International Journal of Fracture 2018;209(1):27-51.

[79] Nguyen HH, Nguyen TN, Vu HC. Ductile fracture prediction and forming assessment of AA6061-T6 aluminum alloy sheets. International Journal of Fracture 2018;209(1):143-162.

[80] Nasir MW, Chalal H, Abed-Meraim F. Formability limit prediction of TRIP780 steel sheet using lode angle dependent gurson-based models with Thomason coalescence criterion and bifurcation analysis. AIP Conference Proceedings 2019;2113.

[81] Nasir MW, Chalal H, Abed-Meraim F. Prediction of forming limits for porous materials using void-size dependent model and bifurcation approach. Meccanica 2020;55:1829-1845.

[82] Mamusi H, Bakhshi-Jooybari M, Gorji H, Hashemi R. A novel experimental approach in determining forming limit diagrams by considering the effect of normal pressure. International Journal of Material Forming 2022;15(1):1.

[83] Hashemi R, Abrinia K. Analysis of the extended stress-based forming limit curve considering the effects of strain path and through-thickness normal stress. Materials & Design 2014;54:670-677.

[84] Abbasi I, Gerdooei M, Nosrati HG. Implementation of the extended maximum force criterion (EMFC) for evaluating the pressure-dependent forming limit diagrams (PD-FLD) in the tube bulging process. The International Journal of Advanced Manufacturing Technology 2025;136(2):863-873.

[85] Ghazanfari A, Soleimani SS, Keshavarzzadeh M, Habibi M, Assempuor A, Hashemi R. Prediction of FLD for sheet metal by considering through-thickness shear stresses. Mechanics Based Design of Structures and Machines 2020;48(6):755-772.

[86] Dewangan YK, Faye A, Bandyopadhyay K. Modeling the through-thickness shear effect in fracture prediction for the SPIF process. Mechanics Based Design of Structures and Machines 2025:1-24.

[87] Samad A, Thakur AK, Basak S, Pal K. Machine Learning Enabled Estimation of Formability for Anisotropic Sheet Metals. Metals and Materials International 2025:1-25.

[88] Sharan SK, Paul SK, Kumari J, Mondal A. Artificial neural network-based prediction of complete forming limit curves for steel in sheet metal forming. Journal of Alloys and Metallurgical Systems 2025;9:100166.

[89] Wang Z, Guines D, Leotoing L. Determination of a machine learning constitutive model from biaxial tensile test: application to thermal forming limits prediction of AA6061 sheets from shear to equi-biaxial tension. In ESAFORM Materials Research Forum LLC 2025;54:1891-1900.

[90] Samad A, Thakur AK, Basak S. Formability prediction of anisotropic thin sheets using machine learning framework: influence of pre-strain and temperature. Journal of Materials Engineering and Performance 2025:1-23.

[91] Sekban DM, Yaylacı EU, Özdemir ME, Yaylacı M, Tounsi A. Investigating formability behavior of friction stir-welded high-strength shipbuilding steel using experimental, finite element, and artificial neural network methods. Journal of Materials Engineering and Performance 2025;34(6):4942-4950.

[92] Sivam SS, Rajendran R. Hybrid optimisation of input process parameters of deep-drawn cylindrical cups from directional rolled copper strips. Proceedings of the Institution of Mechanical Engineers, Part C: Journal of Mechanical Engineering Science 2024;238(8):3259-3272.

[93] Gologanu M, Leblond J-B, Perrin G. A micromechanically based Gurson-type model for ductile porous metals including strain gradient effects. In: Net Shape Processing of Powder Materials 1995;216:47-56.

[94] Benzerga AA. Rupture ductile des tôles anisotropes. Simulation de la propagation longitudinale dans un tube pressurisé. 2000.

[95] Yoon JW, Barlat F, Dick R, Karabin M. Prediction of six or eight ears in a drawn cup based on a new anisotropic yield function. International Journal of Plasticity 2006;22:174-193.

[96] Liu J, Wang Z, Meng Q. Numerical investigations on the influence of superimposed double-sided pressure on the formability of biaxially stretched AA6111-T4 sheet metal. Journal of Materials Engineering and Performance 2012;21:429-436.

[97] Chen Z, Dong X. The GTN damage model based on Hill'48 anisotropic yield criterion and its application in sheet metal forming. Computational Materials Science 2009;44:1013-1021.

[98] Grilo TJ, Valente RA, de Sousa RA. Assessment on the performance of distinct stress integration algorithms for complex non-quadratic anisotropic yield criteria International Journal of Material Forming. 2014;7(2):233-247.

[99] Luo S, Yang G, Lou Y, Xu Y. Prediction of strain path changing effect on forming limits of AA 6111-T4 based on a shear ductile fracture criterion. Metals 2021;11:546.

[100] Zhang R, Shao Z, Lin J. A review on modelling techniques for formability prediction of sheet metal forming. International Journal of Lightweight Materials and Manufacture 2018;1(3):115-125.

[101] Kim J, Gao X. A generalized approach to formulate the consistent tangent stiffness in plasticity with application to the GLD porous material model. International Journal of Solids and Structures 2005;42:103-122.

[102] Tvergaard V, Needleman A. Analysis of the cup-cone fracture in a round tensile bar. Acta Metallurgica 1984;32:157-169.

Graphical Abstract

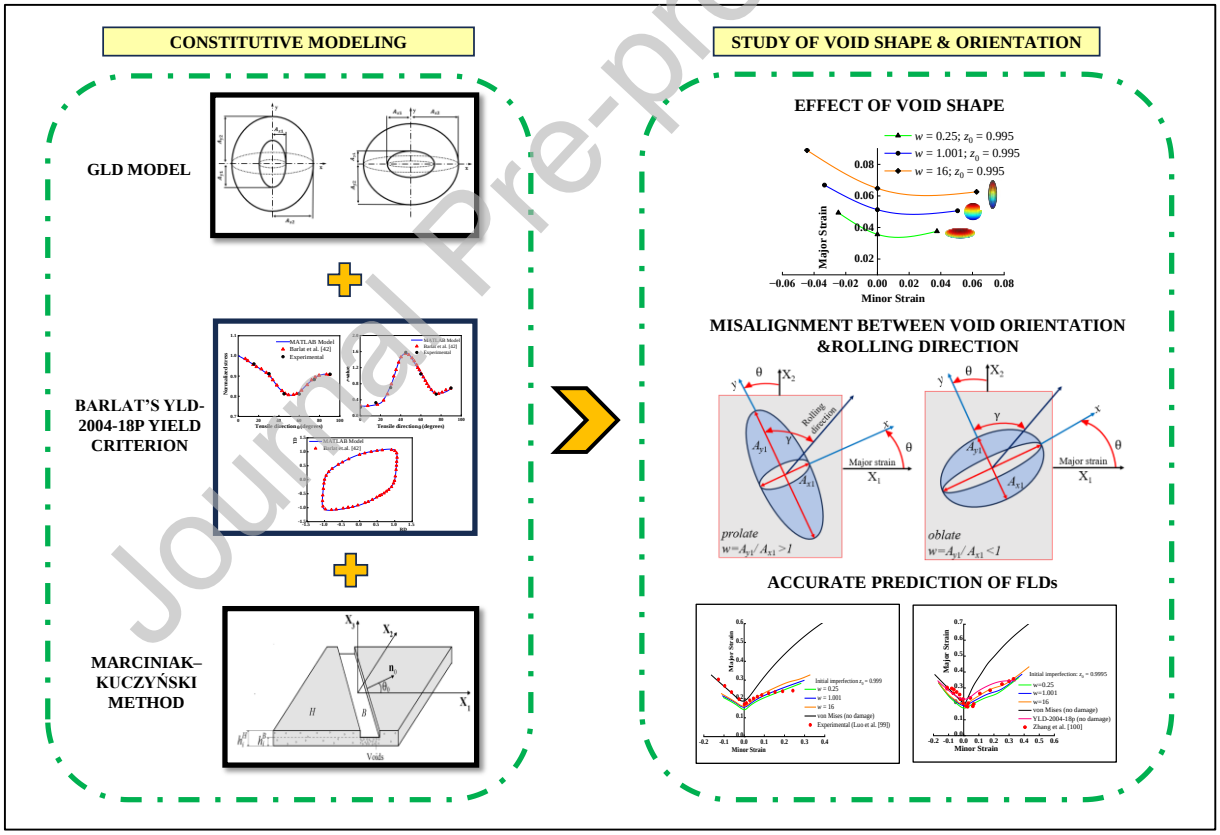

Author Statement